TUDelft

Delft University of Technology

Transient behavior and steady-state rheology of dense frictional suspensions in pressure-driven channel flow

Peerbooms, Wouter; Heijden, Antoine van der; Breugem, Wim Paul

Important note
To cite this publication, please use the final published version (if applicable).
Please check the document version above.

ORIGINAL PAPER

Wouter Peerbooms · Antoine van der Heijden ·
Wim-Paul Breugem

Transient behavior and steady-state rheology of dense frictional suspensions in pressure-driven channel flow

Abstract Results from particle-resolved Direct numerical simulations are presented for dense suspensions of frictional non-colloidal spheres in viscous pressure-driven channel flow. The bulk solid volume fraction varies between $\phi_b = 0.2$ and 0.6, and the Coulomb friction coefficient is either $\mu_c = 0$ or 0.5. The main objectives are to unravel the influence of (1) ϕ_b and μ_c on the flow development time and of (2) heterogeneous shear on the steady-state suspension rheology. Starting from an initially homogeneous distribution, the particles show shear-induced migration toward the core until equilibrium is reached. The flow development time decays exponentially with increasing ϕ_b/Φ_R, where Φ_R is a friction-dependent reference bulk concentration beyond which particle contacts cause a rapid increase in the particle stress. The steady-state rheology is studied by means of the 'viscous' and 'frictional' rheology frameworks. Excluding the central core and wall regions, the data for the local relative suspension viscosity collapse onto a single curve as function of the normalized local concentration $\bar{\phi}/\phi_m$, where ϕ_m is the friction-dependent maximum flowable packing fraction. The frictional rheology shows 'subyielding' at low viscous number I_v in the core region, where the macroscopic friction coefficient μ drops below the minimal value found for homogeneous shear flows. A modified frictional rheology model is presented that captures subyielding. Finally, a model is presented for $\bar{\phi}/\phi_{mp}$ as function of I_v, where ϕ_{mp} is a modified maximum flowable packing fraction. It captures both 'overcompaction' in the core beyond ϕ_m at high ϕ_b and maximum core concentrations below ϕ_m at lower ϕ_b.

1 Introduction

The rheology of dense suspensions is of interest due to the occurrence of suspensions in many natural and industrial applications. One of these applications is the use of suspensions in additive manufacturing, such as for 3D-printing of concrete, metals, food, and energetic materials. The desired solid volume concentration is typically very high for these applications. The complex suspension rheology makes it difficult to control the print quality, especially when the solid volume fraction approaches the maximum flowable packing fraction, ϕ_m.

W. Peerbooms · W.-P. Breugem (✉)
Process and Energy Department, Multiphase Systems, Delft University of Technology, Leeghwaterstraat 39, 2628 CB Delft, The Netherlands
E-mail: w.p.breugem@tudelft.nl

A. van der Heijden
Process and Energy Department, Complex Fluid Processing, Delft University of Technology, Leeghwaterstraat 39, 2628 CB Delft, The Netherlands

A. van der Heijden
Department Energetic Materials, Netherlands Organization for Applied Scientific Research (TNO), Ypenburgse Boslaan 2, 2496 ZA The Hague, The Netherlands

In the present study, we consider the rheology of monodisperse suspensions of non-colloidal and rigid spheres in a Newtonian fluid. Molecular forces, such as Van der Waals forces, electrostatic forces, and Brownian forces, are assumed to be negligible. Such suspensions may exhibit a yield stress, an anisotropic particle stress tensor with normal stress differences, and shear-thickening behavior at high volume fractions [1]. These phenomena are strongly dependent on the solid volume fraction, ϕ, relative to the maximum flowable packing fraction [2]. The closer the volume fraction is to the maximum flowable packing fraction, the more dominant particle contacts are with respect to particle-fluid and hydrodynamic particle-particle interactions. Therefore, particle size, shape, and surface properties become more important in the very dense regime. In this paper, we focus on the influence of solid friction between particles, which is known to have a significant impact on the rheology of dense suspensions [3–8]. Friction also strongly affects the shear-thickening behavior of suspensions [6,7]; however, we will not address the shear-rate-dependent rheology in the current work. The relative suspension viscosity, η/η_0 with η_0 the viscosity of the carrier fluid, is affected by the solid friction through the maximum flowable packing fraction, as the suspension viscosity diverges at a lower solid volume fraction with increasing Coulomb friction coefficient, μ_c [6]. This is in line with the lower maximum packing fraction for particles with a higher friction coefficient [9,10].

Many studies have shown that the relative viscosity as a function of solid volume concentration collapses onto a single curve when the concentration is scaled by the maximum flowable packing fraction [11]. Several models for the relative viscosity have been developed over the years. For dilute suspensions, particle-particle interactions are negligible. The theoretical relation for the relative viscosity by Einstein [12,13] for dilute suspensions gives a linear dependence on the solid volume fraction:

$$\frac{\eta}{\eta_0} = 1 + \frac{5}{2}\phi. \tag{1}$$

For suspensions above a volume fraction of $\phi \approx 0.05$, hydrodynamic particle interactions need to be taken into account. This was analyzed by Batchelor and Green [14], who extended the relation of Einstein with an additional term accounting for hydrodynamic particle pair interactions:

$$\frac{\eta}{\eta_0} = 1 + \frac{5}{2}\phi + \xi\phi^2, \tag{2}$$

where $\xi = 5.2$ for simple shear flows and $\xi = 7.6$ for pure straining flow. However, this relation fails to capture the strong increase in relative viscosity for $\phi \gtrsim 0.1$ [11]. For these higher volume fractions, a theoretical derivation of the relative viscosity becomes increasingly difficult due to the many-body hydrodynamic interactions and contacts.

For the higher volume fractions, quite many empirical correlations exist, such as the relation proposed by Krieger and Dougherty [15]:

$$\frac{\eta}{\eta_0} = \left(1 - \frac{\phi}{\phi_m}\right)^{-2.5\phi_m}, \tag{3}$$

where ϕ_m is typically obtained from a best fit with experimental data. This relation recovers the Einstein viscosity for low volume fractions, but appears not accurate in the very dense limit. Eilers' relation [16] is in good agreement with empirical data for a large range of volume fractions:

$$\frac{\eta}{\eta_0} = \left(1 + \frac{5\phi/4}{1 - \phi/\phi_m}\right)^2. \tag{4}$$

Furthermore, the Maron–Pierce correlation [17] yields good results, especially for high volume fractions [18]:

$$\frac{\eta}{\eta_0} = \left(1 - \frac{\phi}{\phi_m}\right)^{-2}, \tag{5}$$

which is similar to the Krieger–Dougherty relation when $\phi_m = 0.8$, but does not recover Einstein's relation in the dilute regime when $\phi_m \neq 0.8$.

Due to the diverging nature of the relative viscosity at high volume fractions, it is difficult to accurately describe the suspension rheology close to the maximum packing fraction. Therefore, Boyer et al. [18] adopted a frictional rheology description from granular mechanics to describe the dense regime of suspension rheology,

introducing the viscous number I_v as the governing parameter. The viscous number is defined as the ratio of the viscous shear stress over the wall-normal particle stress, $I_v = -\eta_0\dot{\gamma}/\sigma_{p,22}$, with $\dot{\gamma}$ the imposed shear rate and $\sigma_{p,22}$ the normal particle stress in the shear plane. Combining this viscous number with a macroscopic friction coefficient, $\mu = -\sigma_{12}/\sigma_{p,22}$, defined as the ratio of the total shear stress (σ_{12}) over the wall-normal particle stress, results in a description of the rheology that is not hampered by the divergence in the relative viscosity close to the maximum packing fraction. Boyer et al. [18] proposed an empirical relation between the solid volume fraction and the viscous number:

$$\phi(I_v) = \frac{\phi_m}{1 + I_v^n}, \tag{6}$$

with $n = 0.5$ based on a best fit to their experimental data. Furthermore, Boyer et al. [18] proposed a model for the macroscopic friction coefficient according to:

$$\mu(I_v) = \mu_1 + \frac{\mu_2 - \mu_1}{1 + I_0/I_v} + I_v + \frac{5}{2}\phi_m I_v^{1/2}, \tag{7}$$

with $\mu_1 = 0.32$, $\mu_2 = 0.7$, and $I_0 = 0.005$. In Eq. (7), the first two terms correspond to the particle contact contribution, μ^c, whereas the last two terms correspond to the hydrodynamic contribution, μ^h.

Based on the rheological model of Krieger–Dougherty [15], Gallier et al. [5] took a different approach to obtain the hydrodynamic contribution to the macroscopic friction coefficient, which for large values of I_v is approximately given by:

$$\mu^h = I_v + [\eta]\phi_m I_v^{1-n}, \tag{8}$$

with $[\eta] \approx 2.4$ and $n = 0.4$. The value of $n = 0.4$ is also used by Gallier et al. [5] in the relation between the solid volume fraction and the viscous number given by Eq. (6).

The 'viscous' and 'frictional' descriptions of the suspension rheology can be related to each other through $\eta/\eta_0 = \mu/I_v$. By construction, the model of Boyer et al. [18], Eqs. (6) and (7), recovers the correct Einstein limit for $\phi \to 0$ ($I_v \to \infty$) and approaches the Maron–Pierce correlation times the constant μ_1 for $\phi \to \phi_m$ ($I_v \to 0$). Interestingly, based on a Taylor expansion it can be shown that their model also recovers the relation of Batchelor and Green, Eq. (2), for simple shear flows ($\xi = 5.2$) when $\phi_m = 0.697$. The model of Gallier et al. for the hydrodynamic contribution, Eq. (8), does not perfectly recover the Einstein limit for small ϕ as the value for $[\eta]$ is slightly smaller than 2.5, although their model yields a better fit with their data for the higher range of volume fractions considered in their study.

The frictional rheologies of Boyer et al. [18] and Gallier et al. [5] are well defined for simple shear flows, with a uniform shear rate such as encountered in plane Couette flow. However, when pressure-driven channel or tube flow is considered, the shear rate becomes spatially heterogeneous, leading to more complex suspension behavior. Moreover, for an initially homogeneous suspension under shear in the Stokes regime, irreversible multiparticle interactions are responsible for shear-induced particle migration from the high-shear regions at the walls toward the low-shear region around the centerline. This process continues until it is counteracted by particle diffusion in the opposite direction [19]. The shear-induced migration is captured fairly successfully by the suspension balance model (SBM) [20–22]. From a continuum perspective, the particle migration is driven by wall-normal gradients in the wall-normal particle stress [8]. However, literature seems to be inconclusive about the precise origin of the particle stress. For instance, Jamshidi et al. [23] make distinction between the particle-presence stress from hydrodynamic particle interactions and the particle-contact stress from direct particle contacts, and claim that these stresses originate from averaging the momentum equation for the fluid and the particle phase, respectively. This is conceptually different from Morris and Boulay [21], who consider the entire particle stress, including the contribution from hydrodynamic interactions such as lubrication forces, as the result from averaging of the momentum equation for the solid phase only. Furthermore, the SBM relies on the rheological correlations used for the shear and normal particle stresses. In the 'classical' SBM formulation [20], the use of the correlations proposed by Boyer et al. [18] and Morris and Boulay [21] results in an equilibrium concentration distribution with a peak at the centerline equal to the maximum packing fraction, contrary to data from experiments and numerical simulations [8]. As will be discussed later, several remedies have been proposed to overcome shortcomings of the classical SBM formulation [24–27]. Already in the original manuscript in which the SBM was introduced for the first time, Nott and Brady [20] proposed an alternative constitutive relation for the suspension pressure as function of the square root of the granular temperature (a measure for particle velocity fluctuations) to accommodate non-local suspension behavior in

the mean shear rate. This was shown to prevent jamming at the channel centerline, where the mean shear rate reaches zero while the suspension temperature and thus the suspension pressure remain finite.

Next to the modeling of shear-induced particle migration, pressure-driven suspension flows have been studied experimentally for many years [28–34]. Hampton et al. [28] used nuclear magnetic resonance (NMR) imaging to study the migration of particles in pressure-driven tube flow at bulk concentrations up to $\phi_b = 0.5$ and for two different particle-to-tube radius ratios. Particle migration toward the core was responsible for blunting of the streamwise velocity profile. The streamwise development lengths of the velocity and concentration profiles were found to rapidly decrease for increasing concentration and radius ratio, with a more rapid development of the velocity profile compared to the concentration profile. Lyon and Leal [29,30] used laser-Doppler velocimetry (LDV) combined with density and refractive-index matching of the particles with the suspending fluid, in order to investigate the particle migration in plane channel flow. They found good agreement between the experimentally observed velocity profiles and the model predictions; however, the concentration profiles showed larger deviations, especially close to the channel walls, although this was partially ascribed to the inaccuracy of LDV in these regions. Gao et al. [32] used confocal laser scanning microscopy to study the anisotropic suspension structure for pressure-driven flow in microchannels. They found that pair distribution functions obtained from the experiments, were largely in agreement with results from Stokesian dynamics simulations. Evidence was also shown of local ordering (crystallization) of a fraction of the monosized spheres in the core of the channel, where the solid volume fraction reached a peak value of $\phi = 0.564$. Using Magnetic Resonance Imaging (MRI), Oh et al. [33] performed velocity and concentration measurements on suspensions in pressure-driven pipe flow for bulk solid volume fractions up to $\phi_b = 0.55$. Evidence was reported of compaction of the central particle plug beyond the value of the maximum flowable packing fraction, $\phi_m \approx 0.58$, at the plug boundary up to a random close packing fraction, $\phi_{rcp} \approx 0.64$, at the plug center. Moreover, a model was presented for the concentration and velocity profiles based on the mixture momentum balances for the axial and radial directions. A frictional rheology model was employed for the particle stresses, where compaction in the pipe core was accounted for [25]. The model predictions agreed well with the measured blunted velocity profiles and showed compaction of the central particle plug beyond the maximum flowable packing limit, but failed to capture the shape and extent of the central particle plug. More recently, Rashedi et al. [34] used particle image velocimetry (PIV) combined with a refractive-index matching technique, to record the axial development of the concentration profile in a channel flow for concentrations ranging from $\phi_b = 0.1$ to 0.5. Their experiments showed that the maximum volume fraction at the centerline increases with bulk volume fraction and saturates at $\phi \approx 0.6$ for bulk volume fractions beyond $\phi_b = 0.3$. These findings also highlight the discrepancy with the 'classical' suspension balance model, which predicts a centerline volume fraction equal to the maximum packing fraction, ϕ_m, irrespective of the value of ϕ_b.

Numerical simulations of suspension flows have become more feasible over recent years related to the ever increasing computing power, allowing to perform particle-resolved numerical studies on shear-induced particle migration. Yeo and Maxey [35] used a force-coupling method to study the dynamics in plane Poiseuille flow for suspensions of frictionless particles with a bulk concentration in the range of $\phi_b = 0.2 - 0.4$. They observed good agreement of the concentration profiles between their numerical results and the experiments of Hampton et al. [28], Lyon and Leal [29], and Gao et al. [31,32]. Additionally, they showed reasonable agreement between the relative viscosity as a function of the local volume fraction and the earlier mentioned correlations of Krieger and Dougherty [15] and Eilers [16]. A striking observation was the puzzling presence of a negative (positive) particle shear stress just below (above) the channel centerline, opposite to the sign of the local shear rate, and which originated from a negative (positive) contribution from the hydrodynamic particle stresslet. The extension to polydispersity in particle size was studied by Chun et al. [36], using the Lattice-Boltzmann method to simulate segregation of a bidisperse suspension in plane Poiseuille flow at a bulk concentration of $\phi_b = 0.3$. For all investigated particle size and volume fraction ratios, they found that the larger particles preferentially migrate toward the core compared to the smaller particles. The timescale of particle *segregation* appeared to be 5–8 times longer than the timescale for overall particle *migration*, with the latter comparable to the time scale for particle migration in the corresponding monodisperse systems. Di Vaira et al. [37] studied polydisperse systems using a coupled lattice-Boltzmann/discrete-element method. Interestingly, they observed a clear difference in particle segregation for the low and high bulk concentrations investigated: while the larger particles preferentially accumulated in the channel core for $\phi_b \leq 0.3$, there was an increasing preference for the smaller particles to accumulate in the core for $\phi_b \geq 0.4$. The latter was ascribed to the higher shear-rate fluctuations of the smaller particles, which dominate the particle motions in the dense central plug region where the mean shear rate vanishes.

These experimental and numerical studies did not yet lead to a complete description of the suspension dynamics in pressure-driven flows. However, the effort made by Lecampion and Garagash [25] to apply the frictional rheology proposed by Boyer et al. [18] to pressure-driven channel and pipe flow, introduced a clear phenomenological picture of the suspension behavior. Their idea of suspension compaction in the core region was corroborated by the experimental work of Oh et al. [33]. In order to describe this compaction, Lecampion and Garagash [25] proposed a different form of the macroscopic friction coefficient, extending the relation past the maximum flowable packing fraction to account for a jammed particle plug in the center of the channel or pipe:

$$\mu(\phi) = \mu_1 + \frac{\phi_m}{\beta}\left(1 - \frac{\phi}{\phi_m}\right) + \left(I_v + \left(\frac{5}{2}\phi_m + 2\right)I_v^{1/2}\right)\left(1 - \frac{\phi}{\phi_m}\right)^2, \tag{9a}$$

$$I_v(\phi < \phi_m) = \left(\frac{\phi_m}{\phi} - 1\right)^2 \quad \text{and} \quad I_v(\phi \geq \phi_m) = 0, \tag{9b}$$

where $\beta = -d\phi/d\mu$ for $\mu \to \mu_1$ represents the so-called compressibility coefficient and is given a value of 0.158 based on a best fit with experimental data in the dense regime. This model allows μ to decrease below $\mu = \mu_1$ by means of a linear extrapolation of the $\phi(\mu)$ relation for a dense suspension under homogeneous shear toward $\mu = 0$. The maximum possible packing fraction of the particle plug is found from substituting $\mu = 0$ and $I_v = 0$ into Eq. (9a): $\phi_{rcp} = \phi_m + \beta\mu_1$. For $\phi_m = 0.585$, $\beta = 0.158$ and $\mu_1 = 0.3$ (based on a best fit with experimental data), $\phi_{rcp} \approx 0.632$, a value representative for a random close packing of monodisperse spheres. More recently, Chèvremont et al. [38] showed that the separate hydrodynamic and contact contributions to Eq. (9a) do not provide a good description of the frictional rheology in simple shear flow, although the total macroscopic friction coefficient agreed quite well with their numerical simulations.

Based on their proposed frictional rheology model, Lecampion and Garagash [25] also presented analytical solutions for the equilibrium concentration and velocity profiles in fully developed channel and pipe flows. Furthermore, they numerically studied the axial flow development from an initially homogeneous concentration distribution toward equilibrium. The results of these numerical simulations were compared to an analytical expression for the development length, based on the gap-averaged diffusivity evaluated at the channel entrance,

$$L_{\text{dev}} = \frac{2}{3}\frac{I_v(\phi_b)S(\phi_b)}{k(\phi_b)}\frac{H^3}{d^2}, \tag{10}$$

with d the particle diameter, H the channel half-width, ϕ_b the bulk solid volume fraction, $S(\phi) = -(\mu/\phi)(d\phi/d\mu)$ the so-called inelastic storage coefficient, and $k(\phi) = 2f(\phi)/9\phi$ the normalized permeability. The function $f(\phi)$ is based on the empirical hindered-settling function proposed by of Richardson and Zaki [39] and has the form $f(\phi) = (1 - \phi)^n$ with $n \approx 5.1$ used by Lecampion and Garagash [25] for the Stokes regime. Equation (10) showed good agreement with the numerical results over the entire range of solid volume fractions. However, comparison to the experimental pipe flow data of Hampton et al. [28] was less successful for the smaller pipe-to-particle diameter ratio and the lower bulk concentrations, ascribed to a too small particle plug in the pipe core and the related breakdown of the continuum model.

Gillissen and Ness [26] highlighted the two main problems of extending the conventional rheology descriptions for homogeneously sheared flows to flows under heterogeneous shear. For pressure-driven channel flow, flow symmetry and the streamwise momentum balance dictate, respectively, a zero mean shear rate and zero mean total shear stress at the channel centerline. According to the frictional rheology model of Boyer et al. [18] given by Eq. (7), this would imply jamming at $I_v = 0$, $\phi = \phi_m$ and $\mu = \mu_1$, while experimental observations show *subyielding* with $\mu < \mu_1$ for $I_v > 0$ as well as possible *overcompaction* with $\phi > \phi_m$ in the channel core. Gillissen and Ness [26] proposed a rheological model that incorporates shear stress fluctuations to accommodate subyielding and overcompaction, which was in qualitative agreement with particle-based simulation results.

From the above discussion of the literature, it is clear that the rheology of dense suspensions under heterogeneous shear is far from being fully understood. In the present study, we present results from particle-resolved Direct numerical simulations (DNS) for dense suspensions in viscous pressure-driven channel flow. The DNS code is the same as used in our previous study on the rheology of dense suspensions under homogeneous shear [11]. It is based on an efficient Immersed Boundary Method for the fluid/solid coupling [40] and a frictional soft-sphere collision/contact model for particle contacts [41]. We varied the bulk solid volume fraction between $\phi_b = 0.2$ and 0.6. Furthermore, the Coulomb friction coefficient is either $\mu_c = 0$ or 0.5, corresponding to

frictionless and frictional particles, respectively. Our main objectives are to gain insight in the influence of (1) ϕ_b and μ_c on the flow development time and length, and of (2) heterogeneous shear on the steady-state suspension rheology.

Our manuscript is organized as follows. In Sect. 2, we present the governing equations for the suspension flow, the contact model, the numerical method and the computational setup, and we explain the statistical averaging of the DNS data. In Sect. 3, the results are presented. In the first part, we discuss the transient flow behavior and related particle migration toward the core, and we analyze the flow development time and length until statistical equilibrium is reached. In the second part, we discuss the steady-state rheology. We present results for the mean concentration and velocity profiles, the suspension microstructure, and the stress balances for the streamwise and wall-normal directions. We then analyze the 'viscous' suspension rheology in terms of the local relative shear viscosity, η/η_0, as a function of the normalized local mean concentration, $\bar{\phi}/\phi_m$. This is followed by a discussion of the 'frictional' rheology in terms of the macroscopic friction coefficient, μ_c, as a function of the viscous number, I_v. We compare our results with data and models from literature. We present a modified frictional rheology model that accounts for subyielding in the channel core. Furthermore, we introduce a model to relate the local mean concentration to the viscous number through normalization with a *modified* maximum packing fraction, which can capture possible overcompaction in the core region. Finally, in Sect. 4 we summarize our main findings and give recommendations for future research.

2 Methods

2.1 Governing equations and contact model

The fluid phase is governed by the continuity and Navier–Stokes equations that are made dimensionless with the following reference scales[1]: $l_{\text{ref}} = d$, $u_{\text{ref}} = v_{\text{b}}$, $t_{\text{ref}} = l_{\text{ref}}/u_{\text{ref}}$, and $m_{\text{ref}} = \rho_f d^3$, where d is the particle diameter, v_{b} is the bulk mixture velocity, and ρ_f is the fluid phase density.

This leads to the following equations:

$$\nabla \cdot \mathbf{u} = 0, \tag{11a}$$

$$\left(\frac{\partial \mathbf{u}}{\partial t} + \nabla \cdot \mathbf{uu} \right) = -\nabla p_e - \nabla p + \frac{1}{\text{Re}_b(d/2H)} \nabla^2 \mathbf{u}, \tag{11b}$$

in which $\mathbf{u}$ is the velocity, ∇p_e is the pressure gradient used to drive the flow at constant bulk velocity, p is the total pressure minus p_e, and Re_b is the bulk Reynolds number defined as $\text{Re}_b = \rho_f v_b 2 H/\eta_0$ where $2H = L_z$ is the channel height. The particle Reynolds number is based on the wall shear rate of single-phase channel (Poiseuille) flow, $\dot{\gamma}_w = 3v_b/H$, and the particle diameter, and relates to the bulk Reynolds number in the following way:

$$\text{Re}_p = \frac{\rho_f \dot{\gamma}_w d^2}{\eta_0} = \frac{3}{2} \text{Re}_b \left(\frac{d}{H} \right)^2. \tag{12}$$

The particle phase is governed by the Newton–Euler equations:

$$\rho_r \frac{d\mathbf{u}_p}{dt} = \frac{6}{\pi} \left(\oint_{A_p} (\boldsymbol{\sigma}_f \cdot \mathbf{n}) dA + \mathbf{F}_c \right), \tag{13a}$$

$$\rho_r \frac{d\boldsymbol{\omega}_p}{dt} = \frac{60}{\pi} \left(\oint_{A_p} \mathbf{r} \times (\boldsymbol{\sigma}_f \cdot \mathbf{n}) dA + \mathbf{T}_c \right), \tag{13b}$$

in which ρ_r is the ratio between the fluid and solid density; $\mathbf{u}_p$ and $\boldsymbol{\omega}_p$ are the translational and rotational velocity of a particle, respectively; $\boldsymbol{\sigma}_f = -p\mathbf{I} + \frac{1}{\text{Re}_b(d/2H)} \left(\nabla \mathbf{u} + \nabla \mathbf{u}^T \right)$ is the fluid stress tensor; $\mathbf{n}$ is the

---

[1] The inertial scaling of the governing equations in the DNS code was chosen merely for pragmatic reasons as we force a constant bulk velocity in our simulations; hence, a normalized bulk velocity equal to one. The obtained DNS data were rescaled afterward in a viscous manner as appropriate for Stokes flow from a physical standpoint (for example, normalization of stresses by $\eta_0 \dot{\gamma}_w$ instead of $\rho_f v_b^2$).

outward pointing normal vector; and $\mathbf{r}$ is the position vector with respect to the particle centroid. $\mathbf{F}_c$ and $\mathbf{T}_c$ are the force and torque acting on the particle as a result of contacts with other particles or the channel wall.

The fluid and solid phase are coupled through a no-slip/no-penetration condition on the surface of the particles:

$$\boldsymbol{u} = \boldsymbol{u}_p + \boldsymbol{\omega}_p \times \boldsymbol{r} \quad \text{on} \quad A_p. \tag{14}$$

Contact between particles is handled using a soft-sphere contact model including lubrication corrections for short-range particle-particle and particle-wall interactions, which is described in detail by Costa et al. [41]. This contact model is based on a linear spring-dashpot model in which rigid particles are computationally allowed to slightly overlap. The normal contact force is computed from [41]:

$$\boldsymbol{F}_{ij,n} = -k_n \boldsymbol{\delta}_{ij,n} - \eta_n \boldsymbol{u}_{ij,n}, \tag{15}$$

where $\boldsymbol{\delta}_{ij,n}$ is the overlap distance vector between two particles, k_n is the normal spring coefficient, η_n is the normal dashpot coefficient, and $\boldsymbol{u}_{ij,n}$ is the relative velocity vector of the particles in the direction parallel to the line of centers. The effect of solid friction is incorporated in the tangential contact force, including the transition from stick to slip behavior when the tangential-to-normal force ratio exceeds a threshold value [41]:

$$\boldsymbol{F}_{ij,t} = \min\left(||-k_t \boldsymbol{\delta}_{ij,t} - \eta_t \boldsymbol{u}_{ij,t}||, ||-\mu_c \boldsymbol{F}_{ij,n}||\right) \boldsymbol{t}_{ij}. \tag{16}$$

Here $\boldsymbol{\delta}_{ij,t}$ is the tangential displacement, $\boldsymbol{u}_{ij,t}$ is the relative tangential velocity, k_t is the tangential spring coefficient, η_t is the damping coefficient, μ_c is the Coulomb coefficient of sliding friction, and $\boldsymbol{t}_{ij}$ is the surface tangent unit vector.

2.2 Numerical method and computational setup

The governing equations for the fluid phase are solved on a fully staggered, Cartesian grid using a finite-volume/central-differencing approach combined with a predictor/corrector scheme and the third-order three-step Runge–Kutta (RK3) scheme for integration in time. This method is explained in detail by Breugem [40]. For the present simulations in the Stokes regime, the semi-implicit Crank–Nicolson scheme was implemented for integrating the diffusion term in Eq. (11b). An efficient immersed boundary method is used for the fluid/solid coupling, by means of locally adding forces to the Navier–Stokes equations near the boundary of a particle, to enforce Equation (14) by good approximation. As in our previous rheology study [11], the coupling is semi-implicit based on the approach of Tschisgale et al. [42]. The integration of the Newton–Euler equations for the solid phase is performed using the same RK3 scheme, but with substepping for the integration of the contact force and torque to increase the temporal resolution at which particle interactions are resolved [11,41]. For particles in close proximity, lubrication force corrections are used to account for sub-grid hydrodynamic interactions. Interference of the external shear flow with the local lubrication flow is ignored in these force corrections, since the time scale of the external shear flow is much larger than the characteristic time scale for the lubrication flow. Furthermore, as in our previous study [11], the diverging nature of the lubrication force corrections is capped for interparticle distances smaller than $10^{-3}d$ to mimic the effect of surface roughness on the lubrication flow.

The spatial resolution used for the simulations is $\Delta x / d = 1/16$. This resolution was successfully used in the rheological study by Picano et al. [43] for the weakly inertial regime and in our previous work on plane Couette flow in the Stokes regime [11]. The time step used for integration of the Navier–Stokes equations over one full Runge–Kutta integration cycle, was chosen sufficiently small to capture the relevant physical time scales in the suspension flow: $\Delta t \dot{\gamma}_w = 1.56 \cdot 10^{-2}$ and $\Delta t \eta_0 / (\rho_f d^2) = 1.56 \cdot 10^{-3}$. Estimating $\dot{\gamma}_{lub} \sim \dot{\gamma}(d/\Delta x)^{3/2}$ as the typical shear rate of the lubrication flow in between two particles moving at a relative normal velocity $\sim \dot{\gamma}d$ and at one grid cell apart, it follows that $\Delta t \dot{\gamma}_{lub} \sim 1$ in our simulations. Interparticle lubrication is thus resolved in time down to gap widths of $\sim \Delta x$ as desired. To further increase the temporal resolution, substepping has been employed with $\Delta t_{sub} = \Delta t / 40$ for the integration of the lubrication force correction (for interparticle distances well below Δx) as well as for the contact force and the contact torque [11,41].

In this work we consider neutrally buoyant spherical particles that are monodisperse in size. The main parameters that we vary are the bulk volume fraction, which ranges from $\phi_b = 0.2$ to $\phi_b = 0.6$ with increments of 0.1, and the Coulomb coefficient of sliding friction, which is set to $\mu_c = 0$ and $\mu_c = 0.5$ for frictionless and frictional particles, respectively. As specified in Table 1, this gives a total of 10 cases. The same friction
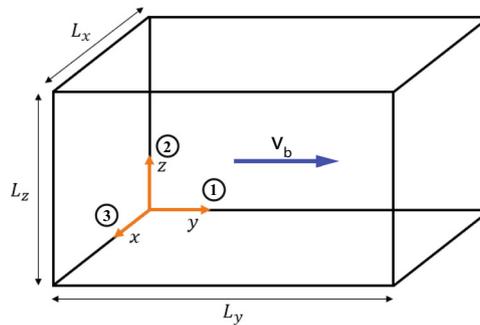
Fig. 1 Schematic of the computational domain with dimensions: $L_x = L_y = L_z = 20d$. Directions are numbered using (1) for the flow direction, (2) for the wall-normal or velocity gradient direction, and (3) for the spanwise or vorticity direction

Table 1 Parameters of the simulated cases: μ_c is the Coulomb coefficient of sliding friction, ϕ_b is the bulk solid volume fraction, N_p is the number of particles, $t_{\text{tot}}v_b/d$ is the total simulated time, $t_{\text{dev}}v_b/d$ is the *estimated* flow development time, "steady state" indicates whether or not fully developed flow was reached, N_{fields} is the number of sample fields in steady state used for statistical averaging, $t_{\text{int}}v_b/d$ is the time interval between the consecutive sample fields, $\overline{\phi_i}$ is the mean solid volume fraction in region i (wall, intermediate, or core region), and z_{core}/d is the wall-normal position at which the core region starts (the upper end of the core region is given by $(L_z - z_{\text{core}})/d$)

μ_c	0					0.5				
ϕ_b	0.2	0.3	0.4	0.5	0.6	0.2	0.3	0.4	0.5	0.6
N_p	3056	4584	6112	7639	9167	3056	4584	6112	7639	9167
$t_{\text{tot}}v_b/d$	3125	5208	5208	2604	2083	3125	5010	3125	2083	1562
$t_{\text{dev}}v_b/d$	12490	11554	4243	1885	1164	10382	4599	2276	1054	458
Steady state	No	No	Yes	Yes	Yes	No	Yes	Yes	Yes	Yes
N_{fields}			180	130	170		80	150	200	200
$t_{\text{int}}v_b/d$			5.21	5.21	5.21		5.21	5.21	5.21	5.21
$\overline{\phi_{wall}}$			0.28	0.40	0.55		0.20	0.28	0.38	0.49
$\overline{\phi_{inter}}$			0.39	0.49	0.61		0.30	0.39	0.48	0.61
ϕ_{core}			0.52	0.59	0.62		0.41	0.51	0.58	0.64
z_{core}/d			6.91	6.53	4.78		7.34	6.66	5.41	3.10

coefficient is used for particle-particle and particle-wall contacts. The computational domain is a square box with dimensions: $L_x = L_y = L_z = 20d$. A schematic of the computational domain is shown in Fig. 1. The domain is periodic in the x and y directions, while having a no-slip/no-penetration boundary condition in the z-direction. The flow is forced by an applied pressure gradient in the y-direction that is dynamically adjusted to enforce a constant mixture bulk velocity. For clarity, the directions are numbered using (1) for the flow direction, (2) for the wall-normal or velocity gradient direction, and (3) for the spanwise or vorticity direction as indicated in the figure. The particle Reynolds number is set to $\text{Re}_p = 0.1$ ($\text{Re}_b = 6.67$) for this study. This value is chosen to be in the Stokes regime while still being high enough for computational efficiency. The particles are initialized by a random positioning in the domain, while making sure there is no overlap between particles and with the wall. For concentrations above $\phi_b = 0.3$, this random initialization is not feasible anymore. Therefore, a body-centered cubic (BCC) structure, with random perturbations in the particle positions, is used for the higher concentrations. The spacing of the BCC structure is adapted to fit the desired number of particles in the domain. The flow is initialized by prescribing a parabolic velocity profile for the fluid and particles corresponding to single-phase plane Poiseuille flow. Additionally, the angular particle velocity is set to half the local fluid vorticity.

The DNS code is written in modern FORTRAN with the MPI extension for parallel computing on multi-core systems with distributed memory. The parallelization consists of a 2D pencil decomposition of the computational domain with a controller-worker technique for handling of the particles. The present simulations were partly run on the Dutch National Supercomputer Cartesius and its successor Snellius and partly on an in-house computer cluster, using 100 and 50 CPU cores per simulation, respectively. In total about ~ 2 million CPU hours were used to run all ten simulations and subsequent postprocessing of the data.

2.3 Statistical averaging

The data generated by the numerical method consist of detailed 3-dimensional velocity and concentration fields. These fields are averaged over space and time to gain useful insights into the mean flow dynamics. For fully developed pressure-driven channel flow, the mean flow and concentration will vary only in the wall-normal direction. Therefore, we apply averaging over thin horizontal slabs with a thickness of 1 grid cell in the wall-normal direction. The so-called superficial averages of the fluid and particle velocities are denoted by brackets and defined by, respectively:

$$\overline{\langle \mathbf{u}_f \rangle}(z) = \overline{\frac{1}{L_x L_y \Delta z} \sum_x \sum_y \mathbf{u}_f(x, y, z, t)\,(1 - \alpha(x, y, z, t))\,\Delta x \Delta y \Delta z}, \tag{17a}$$

$$\overline{\langle \mathbf{u}_p \rangle}(z) = \overline{\frac{1}{L_x L_y \Delta z} \sum_x \sum_y \mathbf{u}_p(x, y, z, t)\alpha(x, y, z, t)\Delta x \Delta y \Delta z}, \tag{17b}$$

where the bar denotes ensemble averaging of samples collected over time. Here α is the solid phase indicator function, which is also used to determine the mean concentration profile as a function of the wall-normal coordinate using:

$$\bar{\phi}(z) = \overline{\frac{1}{L_x L_y \Delta z} \sum_x \sum_y \alpha(x, y, z, t)\Delta x \Delta y \Delta z}. \tag{18}$$

Using the superficial averages and the concentration profile, the so-called intrinsic (phase-averaged) averages can be computed:

$$\overline{\langle \mathbf{u}_f \rangle^f} = \frac{\overline{\langle \mathbf{u}_f \rangle}}{1 - \bar{\phi}}, \tag{19a}$$

$$\overline{\langle \mathbf{u}_p \rangle^p} = \frac{\overline{\langle \mathbf{u}_p \rangle}}{\bar{\phi}}. \tag{19b}$$

In addition to the averaging, the particle stresses need to be computed to describe the rheology of the suspensions. The microscopic particle stress is not explicitly solved in the DNS, but the averaged value within a particle can be computed from the stress distribution on the particle's surface according to:

$$\sigma_{p,ij} \approx \frac{6}{\pi} \left(\oint_{A_p} r_j \sigma_{f,il} n_l \mathrm{d}A + \sum r_j F_{c,i} \right), \tag{20}$$

where the surface integral is equal to the hydrodynamic particle stresslet for freely rotating particles with zero net torque and the summation accounts for the contribution from the particle contacts. Similar to the superficial velocity averages, the superficial particle stress can be determined as a function of the wall-normal coordinate using:

$$\overline{\langle \sigma_{p,ij} \rangle}(z) = \overline{\frac{1}{L_x L_y \Delta z} \sum_{x,y} \sigma_{p,ij}(x, y, z, t)\alpha(x, y, z, t)\Delta x \Delta y \Delta z}. \tag{21}$$

Note that $\sigma_{p,ij}$ at the right-hand side of Eq. (21) is approximated by the *average* stress within a particle and may therefore deviate from the *actual local* stress within a particle when the particle stress distribution is strongly heterogeneous. As a result, the particle stress profiles show artificial oscillations near the wall where the gradients in the solid volume concentration are large due to particle layering.

3 Results and discussion

The investigation of the rheology and the effect of solid friction in pressure-driven plane channel flow can be split in two parts: the transient in which particle migration takes place, and the fully developed flow after the migration is completed. The effect of friction on the particle migration will be discussed first. In this part, we will look at the development of the concentration and velocity profiles as well as the timescale of particle migration. The second part will focus on the description of the rheology of the suspensions in fully developed flow and the effect of solid friction on the rheology. The rheology is studied in terms of velocity and concentration profiles, particle pair distribution functions, stress balances, relative viscosity, normal stress differences, and the frictional rheology.

3.1 Particle migration

The migration of particles in our numerical simulations becomes evident when looking at the spatial particle distribution over time, as shown in Fig. 2. These figures show the particles in a yz cross section of the domain at a fixed x-position for the case with $\phi_b = 0.4$ and $\mu_c = 0$. The time instants for these snapshots are given as a fraction of the time, t_{dev}, for the suspension to become fully developed; the precise definition will be given later. In this case $t = 0.2t_{\text{dev}}$, $t = 0.6t_{\text{dev}}$, and $t = t_{\text{dev}}$ are chosen to show the migration of the particles from an initially homogeneous distribution at $t = 0$. At $t = 0.2t_{\text{dev}}$, it is already visible that the core of the channel is more densely populated by particles, showing that the particles migrated toward the core region where the shear rate is lower. From $0.2t_{\text{dev}}$ to $0.6t_{\text{dev}}$, the most noticeable change is the drop in the number of particles in contact with the wall and the compaction of the suspension in the center of the channel. The color of the particles indicates their streamwise centroid velocity with respect to the mixture bulk velocity. This shows a plug of nearly constant velocity in the channel core, consistent with the high local particle concentration and related suspension viscosity. The core plug becomes thicker over time due to shear-induced particle migration. Outside the plug the particle velocity gradually varies to nearly zero at the walls. Additionally, particle trains are visible where multiple particles are in contact and aligned in an elongated structure. Near the walls, these trains are oriented horizontally as the particles cannot overlap with the wall. Away from the walls, the trains have a predominantly oblique orientation that is caused by the shear-induced interactions between the particles. Close to the centerline, a tendency for a more horizontal alignment is observed again, caused by the low shear rate and larger solid volume fraction in this region. This indicates a microstructure that changes depending on the wall-normal coordinate, which will be investigated in more detail later.

Using averaging over slabs parallel to the walls, we obtained spatially averaged particle concentration and velocity profiles as a function of the wall-normal coordinate that represent the suspension at a particular time instant. From these profiles, the temporal development of the velocity and concentration profiles can be analyzed. For the cases with $\phi_b = 0.4$, which are used as representative cases to show the results throughout this work, the development of the concentration profile is shown in Fig. 3 for frictionless (a) and frictional (b) particles. The volume fraction is normalized by the bulk volume fraction. In both cases, there is a distinct particle layer at the wall. At this bulk volume fraction this layering does not extend into the domain as is the case for higher bulk volume fractions, which will be discussed later. Friction seems to have a pronounced effect on the particles at the wall. In the case with friction, more particles are expelled from the wall layers leading to a lower peak in concentration close to the wall. As seen in the snapshots of Fig. 2, the particles migrate toward the center. The resulting concentration peak in the core is somewhat steeper for the case with friction; however, the development of the peak and its height are similar in both cases. The development of the profiles is in good qualitative agreement with recent results obtained by Orsi [27] for frictional bidisperse sphere suspensions.

To gain more insight into the development of the local solid volume fraction, Fig. 4 shows the local solid volume fraction as a function of the dimensionless time. Three different locations are shown: (1) $z/d = 0.5$, corresponding to the local concentration peak near the wall in Fig. 3, (2) $z/d = 5$, representative for the intermediate region in between the wall and the channel core, and (3) $z/d = 10$, corresponding to the channel centerline. The vertical dashed line shows the overall development time as determined from the evolution parameter discussed later. These figures show that the particle layer at the wall first becomes more densely populated before the local concentration decreases, which is most pronounced for the case without friction. The local concentration in the intermediate region slightly decreases over time as the result of particle migration toward the core. At the centerline, the volume fraction gradually increases until the maximum value is reached,
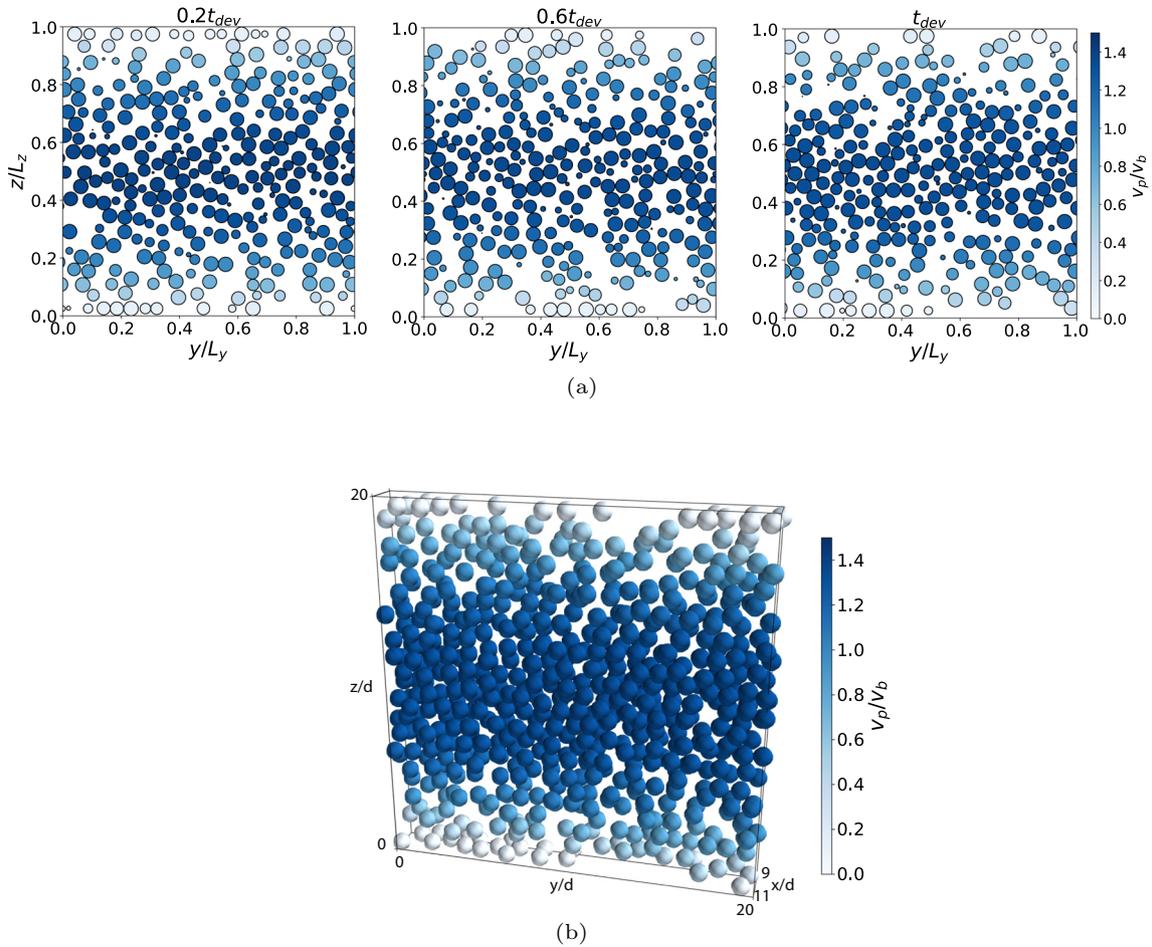
(a)

(b)

Fig. 2 a Particles in a yz cross-section of the domain at a fixed x-position, shown at three different time instants during the development of the flow for the case with $\phi_b = 0.4$ and $\mu_c = 0$. Time is indicated as a fraction of the development time and particles are colored by their streamwise centroid velocity normalized with the mixture bulk velocity. **b** 3D particle distribution around the cross-section shown in (**a**) at $t = t_{\mathrm{dev}}$
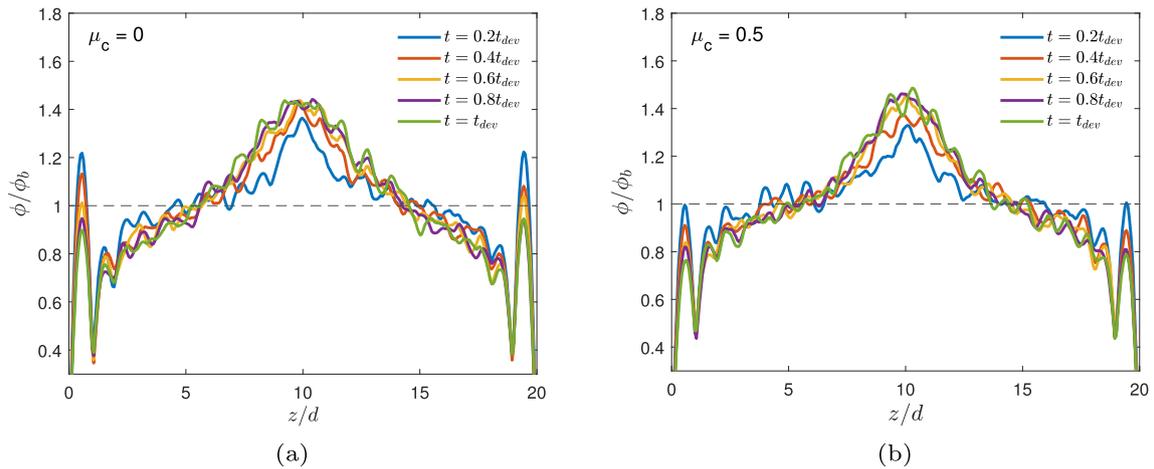

(a)

(b)

Fig. 3 Temporal development of the normalized concentration profile, $\phi(y, t)/\phi_b$, for the cases with $\phi_b = 0.4$, and $\mu_c = 0$ (**a**) and $\mu_c = 0.5$ (**b**)
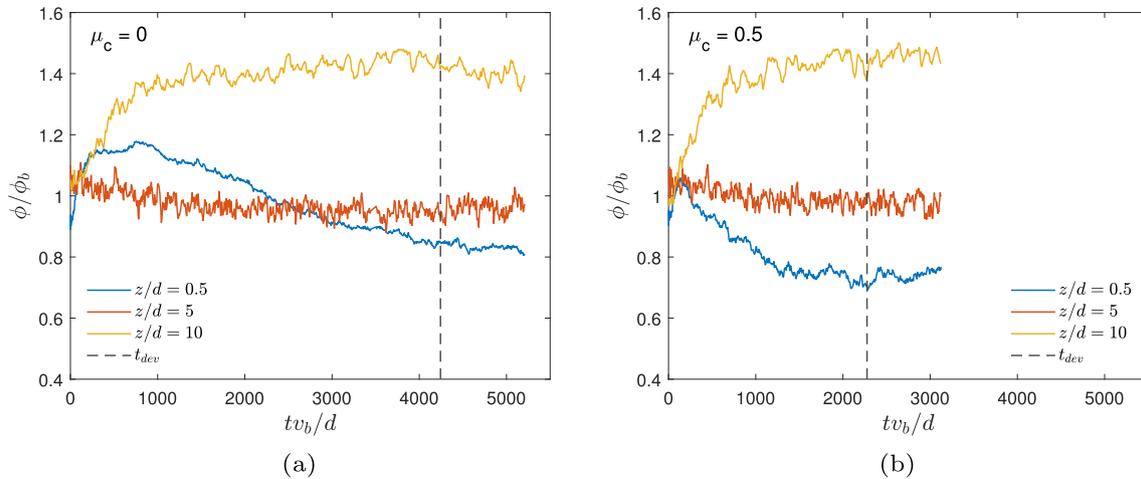
Fig. 4 Temporal development of the normalized concentration profile, ϕ/ϕ_b, for the cases with $\phi_b = 0.4$, and $\mu_c = 0$ (**a**) and $\mu_c = 0.5$ (**b**), shown for three positions in the domain
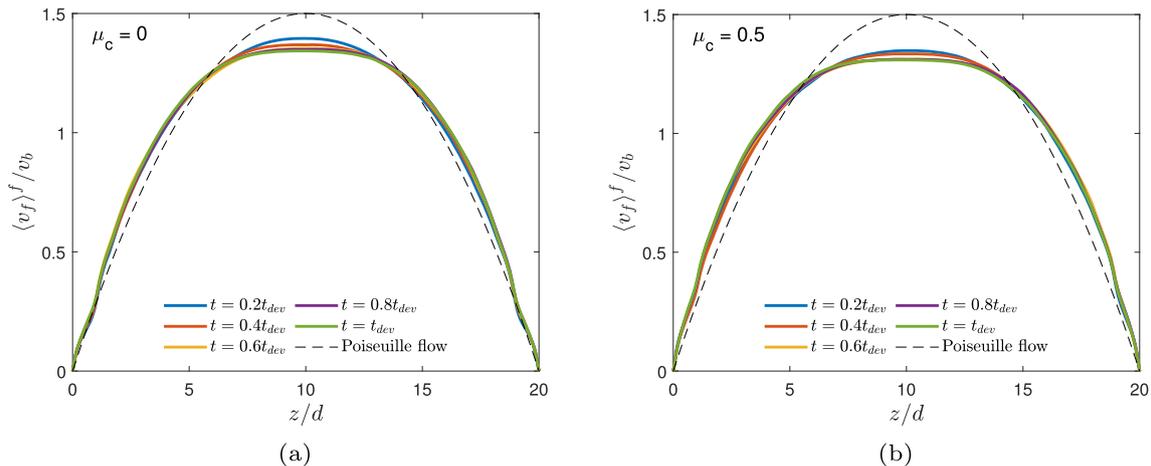

Fig. 5 Temporal development of the intrinsic fluid velocity profile for the cases with $\phi_b = 0.4$, and $\mu_c = 0$ (**a**) and $\mu_c = 0.5$ (**b**)

with a faster development for the case with friction related to stronger shear-induced particle migration. Our results are in good qualitative agreement with the recent work of Orsi [27] for frictional bidisperse sphere suspensions.

The temporal development of the intrinsic fluid velocity profile is shown in Fig. 5 for the cases with $\phi_b = 0.4$. The velocity profile for single-phase Poiseuille flow is shown by the black dashed line as a reference, which is also the initial condition for the suspension velocity. This profile adapts quickly in the first part of the simulations due to the nonzero particle stress distribution as compared to the single-phase counterpart, followed by a slow development due to particle migration. The velocity profile for both cases is blunted with respect to the single-phase profile. Looking more closely at the difference between the two cases, it can be seen that up to $0.2t_{dev}$ the case without friction has a slower initial development compared to the case with friction. The blunted profile shows an area in the center of the channel where the velocity gradient is close to zero, indicating a plug flow behavior. In the case with friction, this plug appears to be slightly wider and has a somewhat lower velocity at all times shown here. Furthermore, these figures show that the development of the velocity profile is much quicker than the development of the concentration profile, as the velocity profile hardly changes anymore after $0.6t_{dev}$. The development of the profiles is in good qualitative agreement with recent results obtained by Orsi [27] for frictional bidisperse sphere suspensions.

From the concentration and velocity profiles we observe that the development of the suspension is affected by the friction coefficient. However, we only looked at a single bulk volume concentration so far. To quantify the effect of the bulk concentration and solid friction on the shear-induced particle migration we analyze the
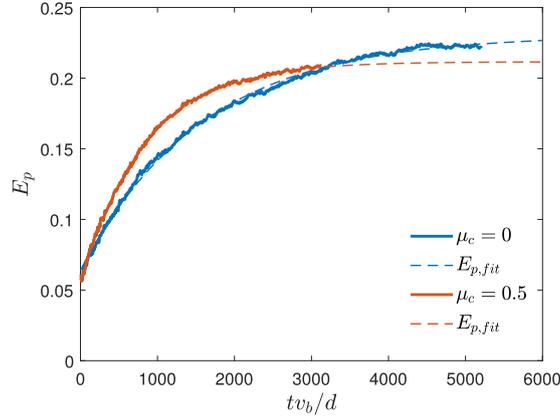
Fig. 6 Evolution parameter as a function of time for the cases with $\phi_b = 0.4$. Dashed lines show fits of Eq. (23) to the data

Table 2 Fitting coefficients for the evolution parameter as defined in Eq. (23)

μ_c	0					0.5				
ϕ_b	0.2	0.3	0.4	0.5	0.6	0.2	0.3	0.4	0.5	0.6
α_1	0.1732	0.2768	0.1665	0.0831	0.1052	0.1663	0.1876	0.1561	0.0896	0.0385
α_2	0.00021	0.00024	0.00063	0.0012	0.0020	0.00024	0.00059	0.0012	0.0023	0.0040
α_3	0.0922	0.0592	0.0640	0.0844	0.1045	0.0972	0.0605	0.0555	0.0703	0.0855

time it takes for the suspension to reach a fully developed state. The development time (t_{dev}) can be determined by means of an evolution parameter defined in a similar way as in Hampton et al. [28]:

$$E_p = \frac{1}{L_z} \int \left| \frac{\phi - \phi_b}{\phi_b} \right| \mathrm{d}z. \tag{22}$$

This evolution parameter measures the deviation of the actual concentration profile from a uniform distribution with a concentration equal to the bulk volume concentration ϕ_b. The evolution parameter can be calculated as a function of time, which is shown in Fig. 6 for the cases with $\phi_b = 0.4$.

To determine the time it takes for the flow to fully develop, we fitted a curve to the data of the form:

$$E_{p,\text{fit}} = \alpha_1 \left(1 - e^{-\alpha_2 t} \right) + \alpha_3, \tag{23}$$

where t denotes the time normalized with d/v_b and α_i are the fitting coefficients. The fitted values of α_i are shown in Table 2. As can be observed from Fig. 6, Eq. (23) provides a very good fit to the temporal evolution of E_p, from which the long-term behavior can be determined even when a simulation is not run until the flow is fully developed.

Following Hampton et al. [28], we define the development time as the moment for which the evolution parameter reaches 95% of its long time plateau value $E_{p,\infty} = \alpha_1 + \alpha_3$. The development time is shown in Fig. 7a as a function of the bulk volume concentration. This shows that the development is faster for the cases with a friction coefficient of $\mu_c = 0.5$ compared to the cases without friction. Furthermore, the development time appears to decay exponentially with the bulk concentration according to:

$$\frac{t_{\text{dev}}}{4H^3/(v_b d^2)} = a e^{-\frac{\phi_b}{\Phi_R}}, \tag{24}$$

where $4H^3/(d^2 v_b)$ is used to normalize the development time based on scaling arguments of Nott and Brady [20], a is a dimensionless constant and Φ_R is a reference bulk volume fraction that depends on the Coulomb friction coefficient. Based on a least-squares fit to the data with $\mu_c = 0.5$, we find that $a = 12.5$. Using this value for a, a least-squares fit gives $\Phi_R = 0.165$ for frictionless and $\Phi_R = 0.127$ for frictional particles. For $\phi_b \gtrsim \Phi_R$, t_{dev} drops significantly below the value $t_{\text{dev}} \approx 12.5 \cdot 4 H^3/(v_b d^2)$ for small ϕ_b. The values found for Φ_R are consistent with the characteristic concentration of roughly 0.1 beyond which particle-particle interactions cannot be ignored anymore and are responsible for the rapid increase in the particle stresses with
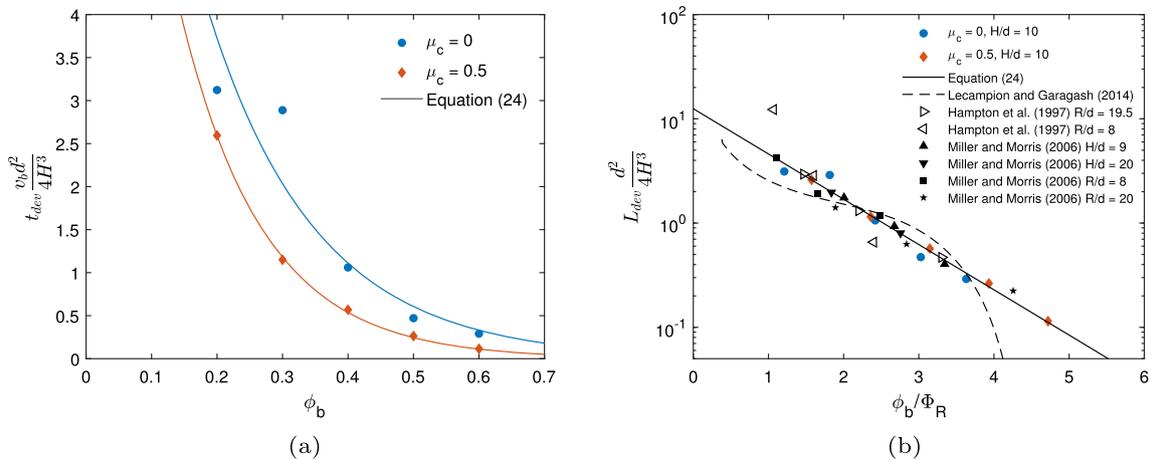
Fig. 7 Timescale of particle migration as a function of the bulk solid volume fraction (**a**) and development length as a function of normalized bulk solid volume fraction (**b**). Development length is compared to the model prediction by Lecampion and Garagash [25] given by Eq. (10), experimental results from Hampton et al. [28] for pipe flow, and numerical results from Miller and Morris [24] for pipe and channel flow. Following Lecampion and Garagash [25], the development length for pipe flow is rescaled to channel flow according to $L_{dev,channel} = 2L_{dev,pipe}$

increasing concentration. As expected, a higher Coulomb friction coefficient corresponds to a lower value of Φ_R, related to faster shear-induced migration due to an enhanced particle stress.

From the development time, the flow development length can be obtained by multiplication with the mixture bulk velocity, $L_{dev} = v_b t_{dev}$. This is normalized with $4H^3/d^2$ [20] and plotted as a function of ϕ_b/Φ_R in Fig. 7b. Here we also include the analytical expression of Lecampion and Garagash [25] given by Eq. (10), the experimental data from Hampton et al. [28] for pipe flow, and the numerical results from Miller and Morris [24] for channel and pipe flow. The corresponding values of Φ_R have been obtained by fitting Eq. (24), with $a = 12.5$ fixed, to the data points and are listed in Table 3. Following Lecampion and Garagash [33], the development length for pipe flow was multiplied with a factor two for comparison with the channel flow data. Figure 7b shows good agreement between the literature data and our numerical results for the range of volume fractions investigated. The analytical expression of Lecampion and Garagash, Eq. (10), is in reasonable agreement with the data $2 < \phi_b/\Phi_R < 4$, but large deviations are present outside this range. Lecampion and Garagash [25] indicate that this discrepancy is caused by the low H/d ratio and low ϕ_b in part of the experiments of Hampton et al. [28] and the related breakdown of the continuum model for the central plug region. However, even for the larger H/d ratio and larger ϕ_b, we see better agreement of the experiments with our fit from Eq. (24) than with their model. This indicates that the development length for shear-induced particle migration can be described by an exponential decay function in the bulk concentration normalized by an appropriate reference volume fraction. Being able to predict this development length is crucial for the design of experiments or numerical simulations where the aim is to study the steady-state behavior of suspensions in pressure-driven flow. Our scaling indicates that $L_{dev}d^2/(4H^3) = 12.5\exp(-\phi_b/\Phi_R)$ is solely a function of ϕ_b/Φ_R and implicitly accounts for Coulomb friction through the value of Φ_R. Dependent on the bulk concentration and the Coulomb friction coefficient, the development length may be well over a factor of 100 smaller for dense suspensions near the jamming limit ($\phi_b \approx 0.6$) compared to dilute suspensions for which $\phi_b \ll \Phi_R$.

According to the suspension balance model [20–22], shear-induced particle migration is caused by the divergence of the wall-normal particle stress, which acts as a force that tends to drive the particles in the direction down the gradient in the absolute stress (i.e., in the direction of the channel core). Therefore, we want to see if there is a difference in this stress for the cases with and without friction, explaining the faster development for the cases with friction. Figure 8 shows the development of the wall-normal particle stress profiles for the cases with $\phi_b = 0.4$. The stress profiles are averaged over 7 sample fields of the flow around the indicated time spaced 1000 timesteps apart, corresponding to an averaging time of $0.009t_{dev}$ and $0.016t_{dev}$ for the frictionless and frictional case, respectively. This averaging is performed to eliminate the largest fluctuations in the stress profiles for the benefit of showing the mean trend over time. The first clear observation is that the magnitude of the wall-normal particle stress is larger for the case with friction. Moreover, the gradients in stress are larger for the case with friction and remain slightly larger when approaching fully developed flow.

Table 3 Values used for normalization of the solid volume fraction with Φ_R for the different datasets in Fig. 7b

Dataset	Φ_R
$\mu_c = 0$	0.165
$\mu_c = 0.5$	0.127
Lecampion and Garagash [25]	0.132
Hampton et al. [28] $R/d = 19.5$	0.136
Hampton et al. [28] $R/d = 8$	0.188
Miller and Morris [24] $H/d = 9$	0.150
Miller and Morris [24] $H/d = 20$	0.163
Miller and Morris [24] $R/d = 8$	0.181
Miller and Morris [24] $R/d = 20$	0.106

R denotes the pipe radius in the pipe flow cases
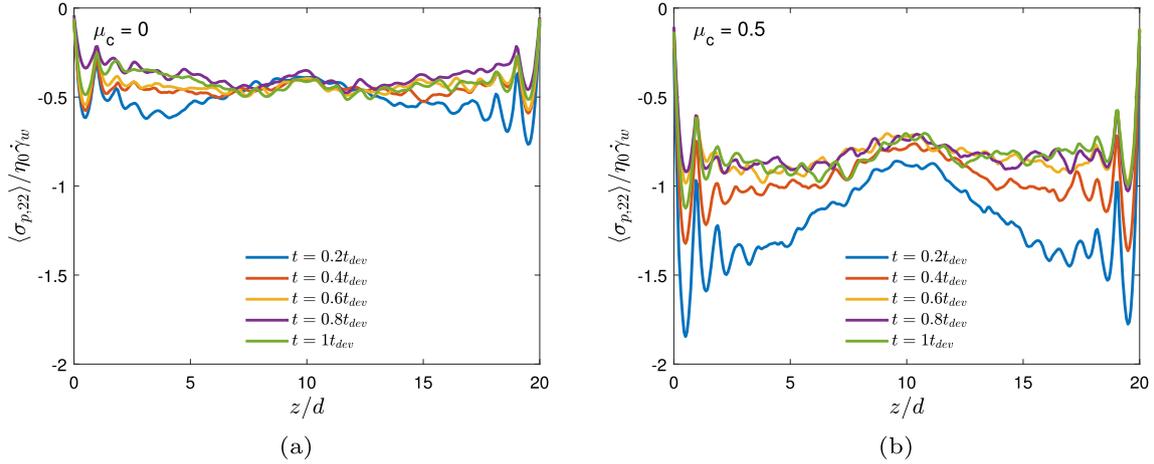
Fig. 8 Development of the superficial wall-normal particle stress profile over time for the cases with $\phi_b = 0.4$, and $\mu_c = 0$ (**a**) and $\mu_c = 0.5$ (**b**). The stress profiles are averaged over 7 sample fields of the flow around the indicated time spaced 1000 timesteps apart, corresponding to an averaging time of $0.009t_{\text{dev}}$ and $0.016t_{\text{dev}}$ for the frictionless and frictional case, respectively

This would indicate a stronger driving mechanism for migration toward the core for the cases with friction, which is in line with our observation for the development length. The development of the wall-normal particle stress shows good qualitative agreement with the results of Orsi [27] obtained for similar suspensions.

3.2 Steady-state rheology

Using the development time determined in the previous section, we can define the moment at which the flow reached a statistically steady state in the simulations in order to study the steady-state rheology of the suspension flow. The steady-state statistics presented in this section are obtained by time-averaging of the plane-averaged fields over a time interval $N_{\text{fields}}t_{\text{int}}$ specified in Table 1. This table also specifies which cases are included in the analysis of the steady-state rheology as it was computationally not feasible to run the cases with the lowest volume fractions until the flow was fully developed. The development time increases exponentially for lower bulk volume fraction and/or higher Φ_R, as is clear from Eq. (24); therefore, we are not able to include the cases with $\phi_b = 0.2$ and the case with $\phi_b = 0.3$ and $\mu_c = 0$.

Steady-state concentration profiles as a function of the wall-normal coordinate are shown in Fig. 9. In these figures, the concentration is normalized by the bulk concentration for easy comparison between the cases. This shows that the peak in the center of the channel deviates more from the bulk volume fraction for lower values of the bulk volume fraction. Furthermore, we observe a stronger wall-induced layering of particles with increasing bulk volume fraction. This layering extends through the entire channel for the cases with $\phi_b = 0.6$. For $\phi_b = 0.6$ and $\mu_c = 0.5$, there is even a crystal structure visible in the center of the channel, which is different than the layering observed at the wall. The crystal structure in the center of the channel corresponds to a body-centered cubic particle arrangement. This actually resembles the initial particle arrangement with
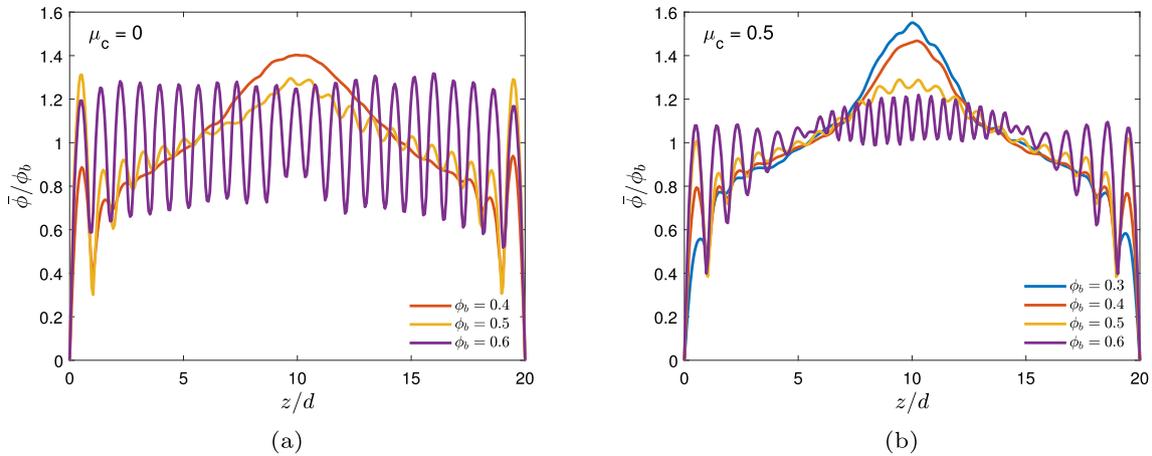
Fig. 9 Steady-state solid volume fraction $\bar{\phi}/\phi_b$ as a function of the wall-normal coordinate for $\mu_c = 0$ (**a**) and $\mu_c = 0.5$ (**b**)
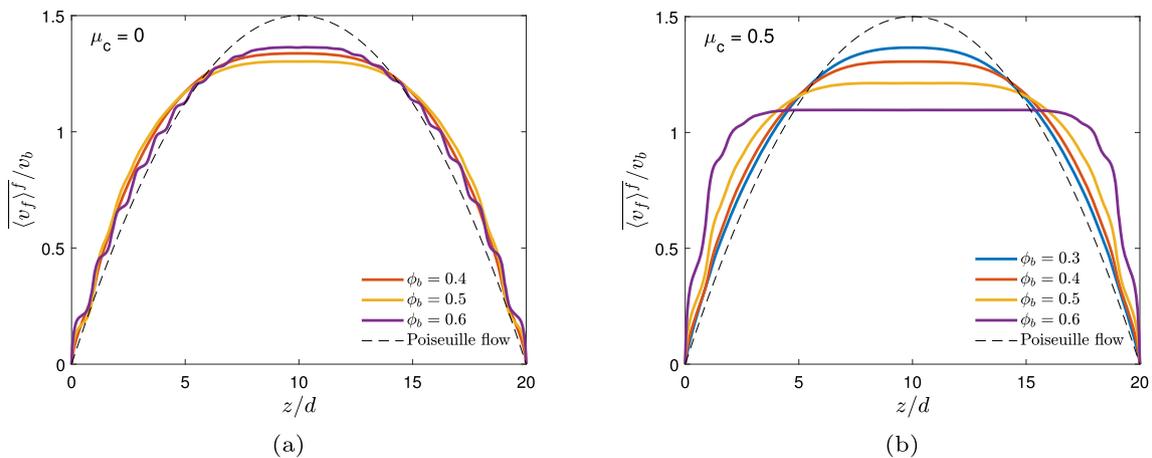

Fig. 10 Steady-state intrinsic streamwise fluid velocity $\overline{\langle v_f \rangle^f}/v_b$ as a function of the wall-normal coordinate for $\mu_c = 0$ (**a**) and $\mu_c = 0.5$ (**b**)

superimposed random perturbations in the particle positions for the cases with $\phi_b > 0.3$, see Sect. 2.2. This shows that at very high bulk concentration, the particles in the channel core do not rearrange but compact into the initial crystal structure. The strong particle layering across the domain severely affects the rheology of the suspensions and is not the focus of the present study. Therefore, we exclude the cases with $\phi_b = 0.6$ from the analysis of the suspension rheology in the remainder of this work.

Steady-state velocity profiles for the same cases are shown in Fig. 10. These figures show that the velocity profile becomes more blunted and has a lower peak value for higher volume fraction with respect to the parabolic profile for a single-phase flow indicated by the dashed line. The region in the center of the channel, where the velocity gradient is zero, is wider for the cases with friction, showing that these suspensions exhibit a stronger plug flow effect. It is interesting to see that the strong layering for the case with $\phi_b = 0.6$ and $\mu_c = 0$ results in a velocity profile closer to parabolic. This might be because the particle layers can more easily slide past each other resulting in a lower particle shear stress and hence suspension viscosity, as was also observed for strongly layered suspensions in simple shear flow [11].

From the concentration and velocity profiles, three distinct regions in the flow can be distinguished. There is a wall region where particle layering, induced by the flat walls, has a large effect on the local concentration. Moving away from the wall toward the center, there is an intermediate region where wall layering is not present and the intrinsic streamwise velocity increases toward the maximum at the centerline. Finally, in the center of the channel, there is a high local concentration and a constant velocity, which is defined as the core region. To take a closer look at the microstructure of the suspension in these three regions, we have computed the particle

pair distribution function (PPDF) defined by:

$$g(\boldsymbol{r}) = \frac{V/V_{vox}}{N(N-1)} \sum_{p} \sum_{p_d} \delta\left(\boldsymbol{r} - (\boldsymbol{x}_{p_d} - \boldsymbol{x}_p)\right), \tag{25}$$

where V is the total volume of the region of interest, V_{vox} is the voxel volume of the regular voxel grid used for the calculation, N is the total number of particles in the region of interest, $\boldsymbol{x}_p$ is the centroid position of the reference particle, and $\boldsymbol{x}_{p_d}$ is the centroid position of a neighboring particle. The function δ gives a value of 1 if the particle centroid of a neighboring particle is in the voxel of interest and 0 otherwise. First, we divide the domain in the three regions mentioned above: the wall region, the core region, and an intermediate region that lies between the two former regions. Based on Figs. 9 and 10, the size of the wall regions is set to three particle diameters from the wall. This is done since wall effects are most pronounced in this region and to ensure that wall effects have minimal effect on the PPDFs of the other two regions. The core region is defined by the plug flow behavior observed in the velocity profiles. The edge of the core region is defined by the position, z_{core}, at which the absolute value of the wall-normal derivative of the plane-averaged streamwise velocity drops below 0.04. This position differs for each case and is therefore determined for all cases separately. An example of the determination of the regions is shown in "Appendix A" for the case with $\phi_b = 0.4$ and $\mu_c = 0$. The PPDFs of the suspensions are calculated for each region separately, where the PPDF for the wall region has been computed for the reference particle located between $1.25 < z/d < 1.75$, approximately corresponding to the second particle layer from the wall. Due to mirror symmetry in the horizontal mid-plane of the channel, the intermediate and wall region PPDFs are mirrored and averaged over the corresponding regions.

The PPDFs for the case with $\phi_b = 0.4$ and $\mu_c = 0$ are shown in Fig. 11, where the red color denotes a higher probability of finding a particle at this position, while the blue color denotes a lower probability relative to a statistically homogeneous particle distribution. Note that the colorbar is split at a value of 1, where the parts above and below both scale linearly but with different factors. The pixelated appearance of the figures stems from the voxel resolution used in combination with the finite number of statistically independent samples.

The PPDF of the wall region nicely illustrates what we observed in the concentration profiles of Fig. 9. By choosing the position of the reference particle in the second layer from the wall, we obtain a clear streak of higher probability at $z/d \approx -1$ corresponding to the layer of particles aligned along the wall. For positive z/d we do not observe layering anymore, as expected from the concentration profile for this case in Fig. 9a, but we find a higher probability in the compressional quadrant of the flow similar to the intermediate region in Fig. 11b. The intermediate region shows clear depletion zones along the extensional axis of the flow around the particle, similar to what is observed from PPDFs for simple homogeneous shear flow [11,44]. Additionally, a lighter streak is visible at a radial position of $r/d \approx 2$ that indicates interactions between multiple particles. This streak is stronger for positive z-coordinates in this figure meaning positions closer to the core of the channel where the suspension is more dense. The PPDF of the core region in Fig. 11c shows high probability zones close to the particle in both the streamwise direction and the wall-normal direction, indicating that contact occurs mostly in these directions. Furthermore, the locally higher probability at $r/d \approx 2$ extends around the entire particle in this region, consistent with the nearly homogeneous concentration in the central plug region.

A convenient way to compare the shear-plane PPDFs of different cases is to radially average the PPDF over a thin shell between $1 < r/d < 1.05$ around the particle as a function of the azimuthal position of the radius vector. This is shown in Fig. 12 for all three regions along the surface of the particle in the shear plane. The cases with $\phi_b = 0.6$ are omitted due to strong wall and initial condition effects, as mentioned before. From the results for the wall region, depicted in Fig. 12a, it is clear that particle layering becomes stronger with increasing bulk volume fraction, which can be seen by the higher peaks at $\theta = 0$, π, and 2π. It seems that the layering starts to become more prominent for $\phi_b > 0.4$, as the results for lower volume fractions show similar behavior. For the cases with $\phi_b = 0.5$, the frictionless case has higher peaks, indicating stronger layering when friction is absent. Common for all cases is a depletion zone around $\theta = 3\pi/4$, which coincides with the extensional quadrant of the flow. If we look at the intermediate region, depicted in Fig. 12b, the first thing that stands out, is that most lines coincide at $\theta = 3\pi/4$ and $\theta = 7\pi/4$. This marks the edge of the depletion zones in the extensional direction of the shear flow, which is very similar to results obtained for simple shear flow [11]. In the depletion zones it can be seen that increasing bulk volume fraction results in a less low probability. Furthermore, the increase in peak height at $\theta = 0$, π, and 2π with bulk volume fraction shows that there is more alignment of particles in the streamwise direction with increasing volume fraction. The effect of friction is not very pronounced in this region, although a slight difference in peak height can be observed, indicating that the frictionless cases exhibit a somewhat stronger alignment in layers. Moving on to the core region, shown in Fig. 12c, we can see a different structure emerging. The depletion zones are absent,
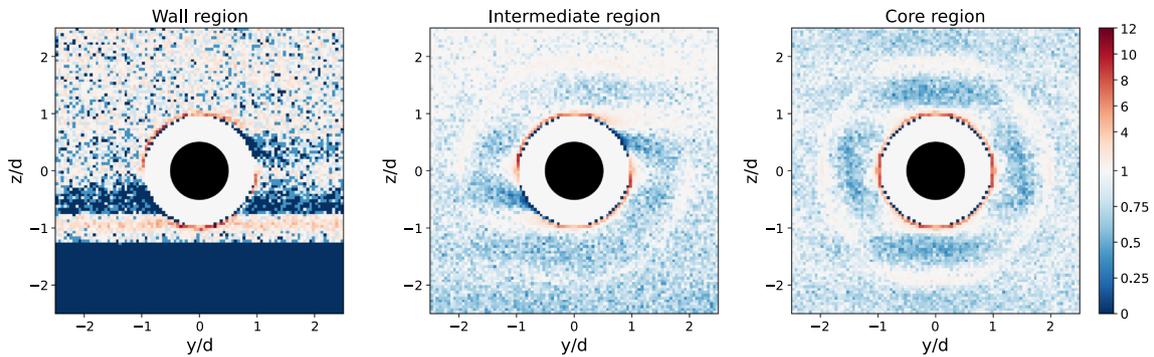
Fig. 11 Steady-state particle pair distribution functions (PPDFs) depicted for the shear plane for $\phi_b = 0.4$ and $\mu_c = 0$, shown for the wall (**a**), intermediate (**b**) and core region (**c**). The black circle in the center marks the reference particle. The white area around this marks the excluded volume where no other particle centroids are found as particles do not overlap. For the wall region PPDF, $z/d = -1.25$ marks the location of the wall when the reference particle is located at a distance of $1.25d$ from the wall, therefore $z/d < -1.25$ is colored blue
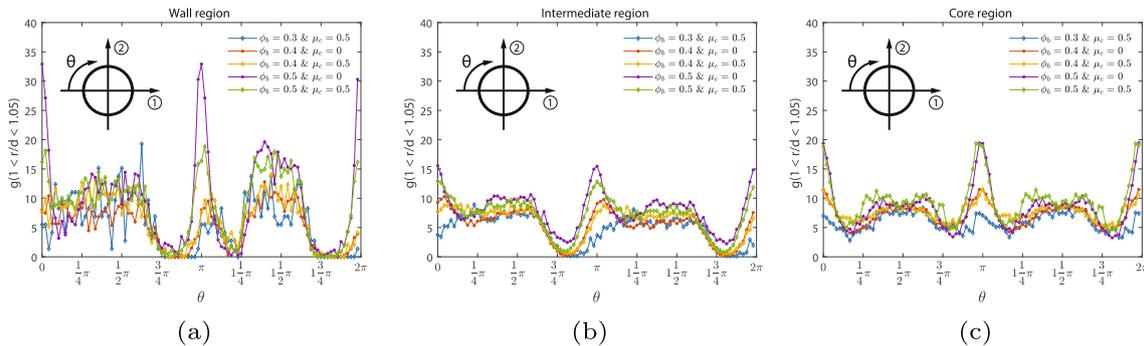
Fig. 12 Steady-state particle pair distribution functions (PPDFs) in the shear plane, averaged over a thin shell around the reference particle ($1 < r/d < 1.05$), shown for all cases in the wall (**a**), intermediate (**b**), and core (**c**) regions

and there is a strong increase in peak height for increasing volume fraction. The absence of depletion zones can be explained by the plug flow behavior that we observed in the velocity profiles, corresponding to a zero mean shear rate in the core. This results in the collective movement of particles with the mean flow, instead of particles moving past each other in layers with different velocities. The higher peaks at $\theta = 0, \pi$, and 2π with increasing bulk volume fraction show that there is stronger alignment of particles in the streamwise direction. There seems to be no difference with regard to friction, indicating that the microstructure is similar in the core region of the flow for frictionless and frictional cases.

From the mean concentration profiles and the suspension microstructure, it becomes evident that the suspensions are not uniformly distributed. This inhomogeneity complicates the calculation of the rheology of the suspensions, because the rheology is dependent on the volume fraction, which changes throughout the channel. Therefore, we study the local rheology of the suspensions in relation to the local volume fraction. To calculate the local rheology, the stresses as a function of the wall-normal coordinate are required. For the Stokes flow regime, the stress balance for the streamwise direction can be written as (see, e.g., [8]):

$$\frac{1}{\mathrm{Re}_b(d/2H)}\frac{\partial \overline{v_m}}{\partial z} + \overline{\langle \sigma_{p,12} \rangle} = (z - z_{\mathrm{core}})\overline{\frac{\partial p_e}{\partial y}}, \qquad (26)$$

where the left-hand side is the total shear stress, $\overline{\langle \sigma_{12} \rangle}$, consisting of the viscous and the particle shear stress, respectively, and $\overline{v_m} = \langle v_f \rangle + \langle v_p \rangle$ is the mean mixture velocity of the suspension. The different stress contributions in this equation are shown in Fig. 13a as a function of z/d for the case with $\phi_b = 0.4$ and $\mu_c = 0$, where the stress is normalized using the viscous wall shear stress for single-phase Poiseuille flow ($\eta_0 \dot{\gamma}_w$). The total stress coincides with the expected stress determined from the pressure gradient in almost the entire channel, with small deviations close to the wall related to a bias in the reconstruction of the particle stress in a strongly heterogeneous flow, as discussed in Sect. 2.3. The particle stress $\overline{\langle \sigma_{p,12} \rangle}$ has the largest contribution to
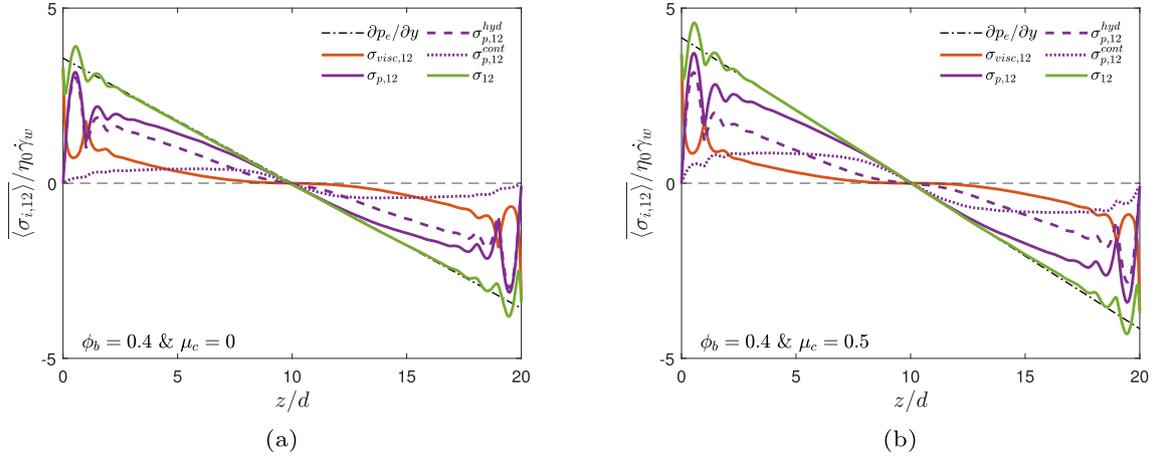
Fig. 13 Steady-state mean superficial shear stress $\overline{\langle \sigma_{i,12} \rangle}$ as a function of the wall-normal coordinate for $\phi_b = 0.4$ with $\mu_c = 0$ (**a**), and $\mu_c = 0.5$ (**b**). Different colors indicate the various stress terms, while the dashed and the dotted line show the hydrodynamic and the contact contribution to the particle stress, respectively. The dash-dotted line shows the total shear stress distribution expected from the balance with the mean streamwise pressure gradient, $(z - z_{\text{core}})\overline{\partial p_e / \partial y}$

the total shear stress in this case, in particular in the core region where the particle concentration is highest. As in our previous study on simple shear flows [11], the particle stress can be decomposed into a hydrodynamic contribution, $\overline{\langle \sigma_{p,12}^{\text{hyd}} \rangle}$, and a contact contribution, $\overline{\langle \sigma_{p,12}^{\text{cont}} \rangle}$, which are shown by the dashed and the dotted line, respectively. Here the lubrication force corrections, discussed in Sect. 2.1, are included in the hydrodynamic contribution of the stress. The hydrodynamic contribution dominates over the contact contribution in the wall region, while the opposite is true for the dense core region where the contact contribution is highest. Contrary to the findings of Yeo and Maxey [35] for frictionless particles, we do neither observe a transition from positive to negative particle shear stress in the core region *below* the channel centerline nor an accompanying sign change in the hydrodynamic contribution; the particle shear stress only changes sign *at* the channel centerline. The reason for the different findings of Yeo and Maxey [35] for the particle shear stress remains puzzling.

The frictional case with $\phi_b = 0.4$ and $\mu_c = 0.5$ is shown in Fig. 13b. The shear stress shows a small increase in the presence of particle friction for this case. This increase is caused by the increase of the contact contribution of the particle stress, which is still more or less uniform in the intermediate flow region but has a larger magnitude compared to the case without friction. Looking at the stress balance for the other cases (not shown), we observe a larger magnitude of the total shear stress for higher bulk volume fraction, resulting from a larger contribution of the particle stress component and with a stronger effect in the cases with friction resulting from an increase in the contact contribution. These stress profiles show good qualitative agreement with the results of Orsi [27] for frictional bidisperse suspensions.

From the shear stress balance, we can determine the relative shear viscosity of the suspensions as a function of the wall-normal coordinate. The relative shear viscosity is defined here as the local total shear stress over the local viscous shear stress according to:

$$\frac{\eta}{\eta_0} = 1 + \frac{|\overline{\langle \sigma_{p,12} \rangle}|}{\frac{1}{\text{Re}_b (d/2H)} \left| \frac{\partial \overline{v_m}}{\partial z} \right|}. \tag{27}$$

For the calculation of the relative viscosity, a region of 2 particle diameters wide is excluded near the channel walls, which is affected by the nearby presence of the wall. Additionally, the region where the viscous shear stress becomes close to zero near the centerline is excluded as well. An example of the relative viscosity calculation is shown in "Appendix B" for the case with $\phi_b = 0.4$ and $\mu_c = 0$. Knowing the relative shear viscosity and the local solid fraction as a function of the wall-normal coordinate, we can combine the two to obtain the relative shear viscosity as a function of the local solid volume fraction. This is shown in Fig. 14a. This shows that the cases with different bulk volume concentration exhibit similar relative viscosity curves if the local volume fraction is considered. The viscosity diverges at high volume fractions and this divergence occurs at lower local volume fraction for the cases with solid friction. These results are in line with results for the relative viscosity found in literature for simple shear flows [8,11]. Looking at the range of local
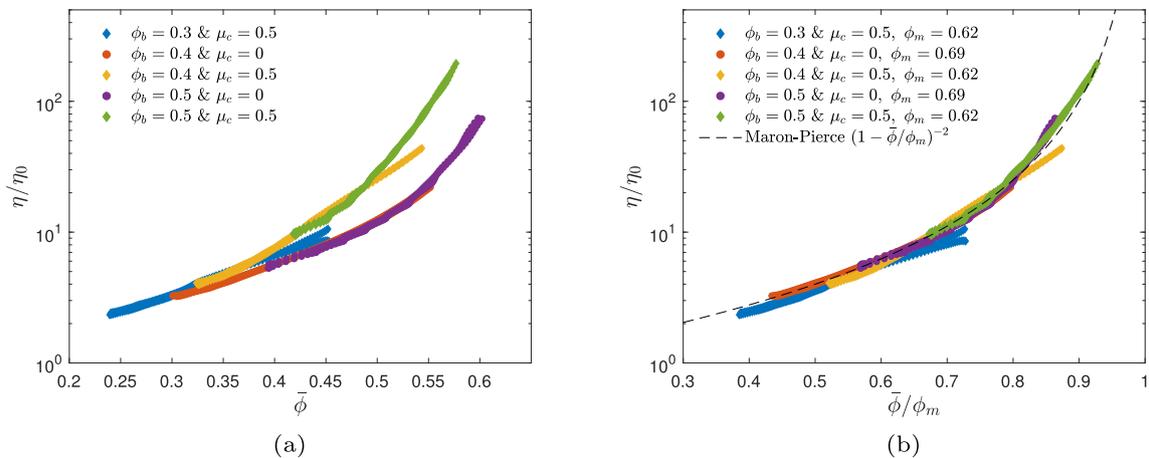
Fig. 14 Local relative shear viscosity as a function of the local volume fraction (**a**) and as a function of the local volume fraction normalized by the maximum flowable packing fraction (**b**). The maximum packing fraction is determined by fitting the Maron–Pierce correlation [17] given by Eq. (5) to all data with the same Coulomb friction coefficient

volume fractions observed in each case, we can see a shift to higher local volume fractions with increasing bulk volume fraction. As discussed in the introduction section, it is well known from literature that the relative shear viscosity collapses onto a single curve when the volume fraction is normalized by the maximum flowable packing fraction. To test this for our data, we fitted the Maron–Pierce correlation [17], Eq. (5), to all data for each friction coefficient to determine the maximum flowable packing fraction. From the results, shown in Fig. 14b, we observe excellent collapse onto a master curve when the volume fraction is normalized by ϕ_m. The maximum flowable packing fractions are $\phi_m = 0.69$ for the frictionless cases and $\phi_m = 0.62$ for the frictional cases, indicating that the maximum flowable packing fraction decreases with increasing friction coefficient, as expected [11]. These results are in line with results from literature and show that the local relative viscosity in the intermediate regions (i.e., between the core and walls) of pressure-driven channel flow behaves similar to the relative viscosity behavior observed in simple shear flow [11].

To investigate the divergence of the relative viscosity at large concentration and the effect of friction more closely, the contributions to the total shear stress are separated in the calculation of the viscosity. This results in a hydrodynamic (i.e., the contributions from the viscous stress and the hydrodynamic part of the particle stress) and contact contribution, which are shown in Fig. 15. The hydrodynamic part coincides for all cases as a function of the local volume fraction as shown in Fig. 15a, whereas the contact part falls onto two different branches corresponding to the two different values of the solid friction coefficient. When the local volume fraction is normalized by ϕ_m, as done in Fig. 15b, the hydrodynamic part shows a poorer collapse while the contact part shifts toward a single curve. This shows that the hydrodynamic part scales with the local volume fraction itself, irrespective of the solid friction, whereas the contact part scales with the local volume fraction normalized with ϕ_m and is strongly affected by solid friction. From this figure, it is also clear that the contacts start to dominate the rheology at a volume fraction of $\bar{\phi}/\phi_m \approx 0.7$, which is in line with previous observations for simple shear flow [11].

To obtain more insight in the suspension rheology, we also studied the normal stresses and in particular the wall-normal stress. The stress balance for the wall-normal direction is written as:

$$- \overline{\langle p \rangle} + \overline{\langle \sigma_{p,22} \rangle} = \text{const.,} \tag{28}$$

where the left-hand side represents the total normal stress, $\overline{\langle \sigma_{22} \rangle}$. The fluid pressure is defined relative to the average wall pressure in the simulations, hence $\overline{\langle p \rangle} = 0$ at the walls, and the constant in Eq. (28) is thus equal to the wall-normal particle stress at the walls. Figure 16 shows the pressure and the wall-normal particle stress for the cases with $\phi_b = 0.4$. Here, we observe that the total normal stress is constant in the center of the channel, as expected, while oscillations are visible near the walls related to the bias in the reconstruction of the particle stress mentioned before. A more accurate determination of the particle stress at the wall, based on the average particle/wall contact force per unit area, is shown by the black dash-dotted line and shows perfect agreement with the value of the wall-normal stress in the core. The total normal stress is dominated by the contribution from the normal particle stress, while the contribution from the fluid pressure is comparatively
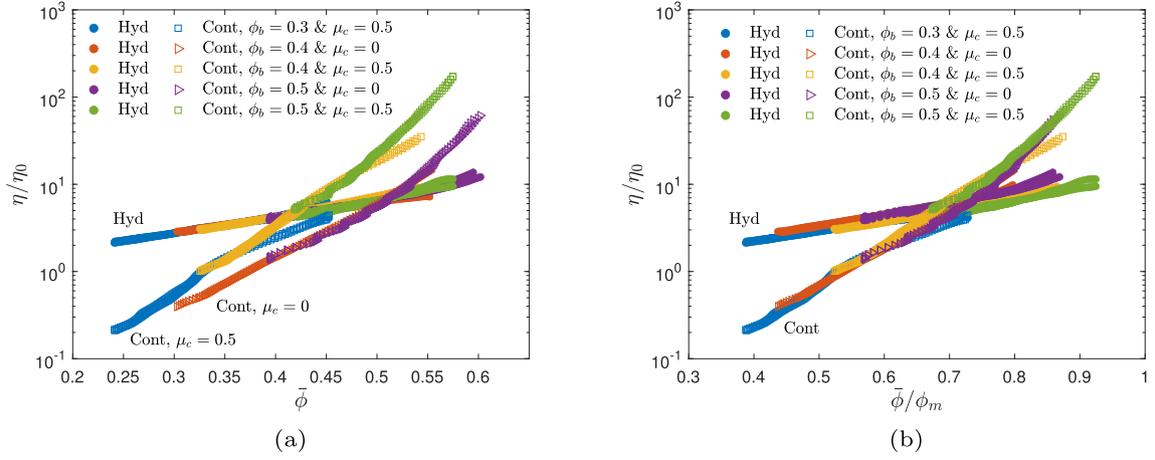
Fig. 15 Decomposition of the local relative shear viscosity into a hydrodynamic and a contact contribution as a function of the local volume fraction (**a**) and of the local volume fraction normalized by the maximum flowable packing fraction (**b**)
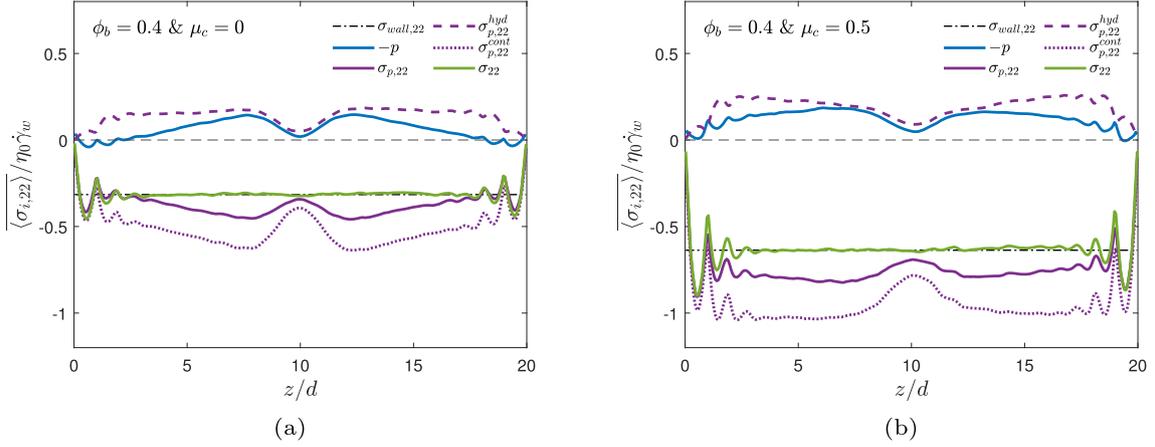

Fig. 16 Steady-state mean superficial wall-normal stress $\overline{\langle \sigma_{i,22} \rangle}$ as a function of the wall-normal coordinate for $\phi_b = 0.4$ with $\mu_c = 0$ (**a**), and $\mu_c = 0.5$ (**b**). Different colors indicate the various stress terms, while the dashed and the dotted lines show the hydrodynamic and the contact contribution to the particle stress, respectively. The black dash-dotted line is the wall-normal stress computed from the average particle/wall contact force per unit wall area

smaller in magnitude and has the opposite sign. The decomposition of the particle stress shows that the contact contribution is dominant, while the hydrodynamic part has the opposite sign and is of the same order as the fluid pressure. The magnitude of the total wall-normal stress increases in the presence of solid friction, as shown in Fig. 16b. This increase is mostly accounted for by an increase in the contact contribution to the particle stress, as observed before for the increase in the total shear stress in the presence of solid friction. Looking at all the cases (not shown), we observe that the magnitude of the wall-normal stress increases with increasing volume fraction and the effect of friction is present for all volume fractions considered here.

The anisotropy of the microstructure of the suspension induces anisotropy in the normal particle stresses [8], a feature of non-Newtonian behavior. The local normal particle stresses normalized by the local total shear stress are shown in Fig. 17 for all three directions. Correlations introduced by Badia et al. [45] are fitted to the data and are given by:

$$\frac{\overline{\langle \sigma_{p,11} \rangle}}{|\langle \sigma_{12} \rangle|} = a_1 \left(\frac{\bar{\phi}}{\phi_m} \right)^{a_2}, \tag{29a}$$

$$\frac{\overline{\langle \sigma_{p,22} \rangle}}{|\langle \sigma_{12} \rangle|} = \frac{\overline{\langle \sigma_{p,11} \rangle}}{|\langle \sigma_{12} \rangle|} \left(b_1 + b_2 \frac{\bar{\phi}}{\phi_m} + b_3 \left(\frac{\bar{\phi}}{\phi_m} \right)^2 \right), \tag{29b}$$
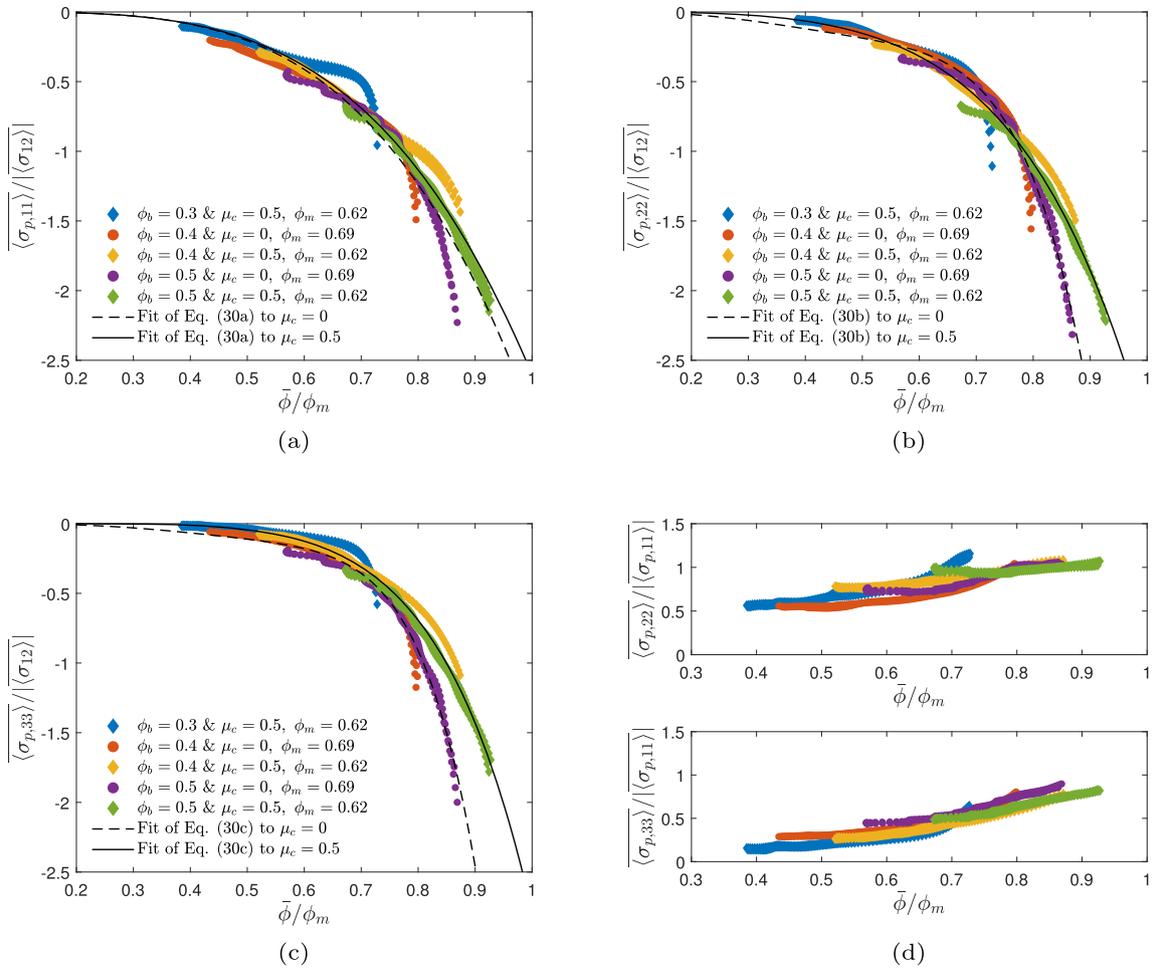
Fig. 17 Normal particle stresses $\overline{\langle \sigma_{p,ii} \rangle}$ as a function of the normalized local solid volume fraction in the streamwise (**a**), wall-normal (**b**), and spanwise (**c**) directions, as well as the ratios λ_2 and λ_3 (**d**). Lines indicate fits of Eq. (29) to the data with $\mu_c = 0$ (dashed) and with $\mu_c = 0.5$ (solid)

$$\frac{\overline{\langle \sigma_{p,33} \rangle}}{|\overline{\langle \sigma_{12} \rangle}|} = \frac{\overline{\langle \sigma_{p,11} \rangle}}{|\overline{\langle \sigma_{12} \rangle}|} \left(c_1 + c_2 \frac{\bar{\phi}}{\phi_m} + c_3 \left(\frac{\bar{\phi}}{\phi_m} \right)^4 \right). \tag{29c}$$

Here a_i, b_i, and c_i are the fitting coefficients for which the values are shown in Table 4. The values for ϕ_m are based on the fit of the Maron–Pierce correlation shown in Fig. 14b. The correlations are fitted to the data for $\mu_c = 0$ and $\mu_c = 0.5$, which are shown in Fig. 17 as the dashed and solid black lines, respectively. These fits show a good description of the data with some deviations at high volume fractions. However, the distinction between the two solid friction coefficients is captured well. Figure 17d shows the ratios of the normal stress components, $\lambda_2 = \overline{\langle \sigma_{p,22} \rangle} / \overline{\langle \sigma_{p,11} \rangle}$ and $\lambda_3 = \overline{\langle \sigma_{p,33} \rangle} / \overline{\langle \sigma_{p,11} \rangle}$. These ratios show little dependence on the friction coefficient and more or less collapse to a single curve. Both λ_2 and λ_3 increase with increasing volume fraction, with λ_2 being consistently larger than λ_3.

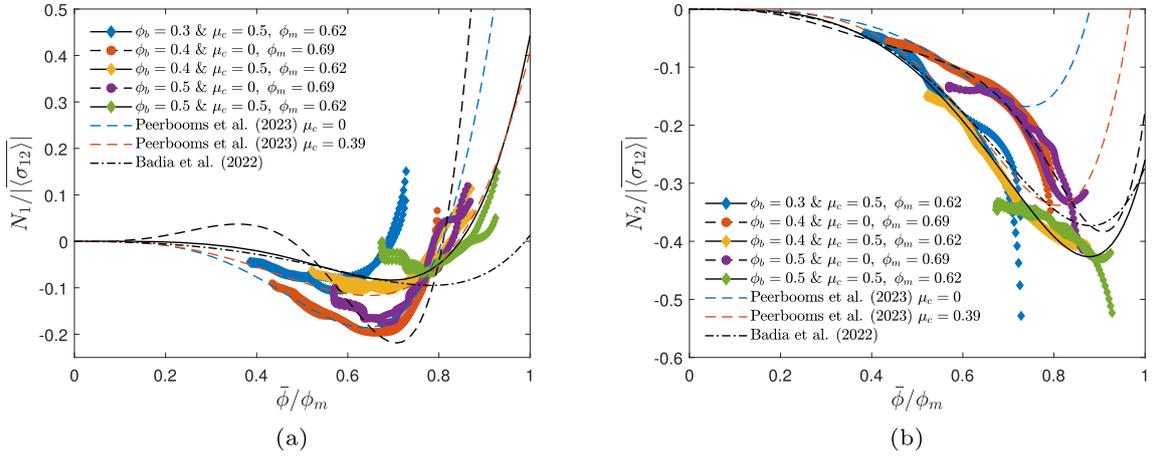From the normal stresses, the normal stress differences can be determined. These are defined as:

$$N_1 = \overline{\langle \sigma_{p,11} \rangle} - \overline{\langle \sigma_{p,22} \rangle}, \tag{30a}$$

$$N_2 = \overline{\langle \sigma_{p,22} \rangle} - \overline{\langle \sigma_{p,33} \rangle}. \tag{30b}$$

Figure 18 shows the local normal stress differences normalized by the local shear stress as a function of the normalized volume fraction. The data fall on two separate master curves for the two solid friction coefficients. For the first normal stress difference, shown in Fig. 18a, we observe slightly negative values with an increase at high volume fraction going to positive values. This behavior was also observed for simple shear flow [11],

Table 4 Fitting coefficients for the correlations describing the normal stresses as defined in Eq. (29) compared to the coefficients found in previous work on simple shear flows by Peerbooms et al. [11] and by Badia et al. [45]

| | $\mu_c = 0$ | $\mu_c = 0.5$ | Peerbooms et al. [11] | | | Badia et al. [45] |
			$\mu_c = 0$	$\mu_c = 0.2$	$\mu_c = 0.39$	
a_1	-2.9046	-2.6033	-2.3022	-2.3305	-2.3648	-2.4247
a_2	3.8209	3.7262	2.7915	2.9724	3.0688	4.1280
b_1	5.6457	0.8698	0.9717	0.5938	0.3792	2.1446
b_2	-15.4846	-0.6578	-2.0377	-0.2760	0.4415	-2.7234
b_3	12.0409	0.9583	2.5687	0.9074	0.3524	1.5759
c_1	2.0493	-0.1410	0.5895	0.4977	0.3361	0.3750
c_2	-3.4621	0.6552	-0.5932	-0.3755	-0.0983	0.0366
c_3	3.5545	0.5564	1.8373	1.2661	1.0189	0.4846

Fig. 18 First (**a**) and second (**b**) normal stress difference as a function of the normalized local solid volume fraction. Black dashed and solid lines show normal stress differences based on fits of Eq. (29), colored dashed lines are results from Peerbooms et al. [11] for simple shear flow, and the dash-dotted line shows a correlation from Badia et al. [45]

which is shown as the colored dashed lines. The blue dashed line corresponds to simple shear flow of frictionless particles [11] and matches very well with our data. The same holds for the frictional case shown by the red dashed line, even though the friction coefficient is slightly different in those simulations with $\mu_c = 0.39$. From the correlations in Eq. (29), we can also compute the normal stress differences, shown here by the dashed and solid black lines for frictionless and frictional cases, respectively. These show a somewhat less accurate match with the data compared to the data from simple shear flow, especially for the case without friction. Looking at the second normal stress difference, shown in Fig. 18b, the distinction between the two friction coefficients is very clear. N_2 is negative with increasing magnitude for increasing volume fraction. The normal stress differences computed from the fits of Eq. (29) show very good agreement with the data, showing that the correlations for $\overline{\langle\sigma_{p,22}\rangle}$ and $\overline{\langle\sigma_{p,33}\rangle}$ are accurate. The lines describing the simple shear flow [11] show good agreement for low volume fractions but show a stronger upswing close to the maximum packing fraction. The dash-dotted line shows a correlation by Badia et al. [45] that was fitted to data compiled from a number of literature sources [5,46,47], which matches the general behavior of our data for both normal stress differences quite well.

As discussed in the introduction section, an alternative method to describe the rheology of suspensions was introduced by Boyer et al. [18], in which the so-called viscous number is used as a governing parameter to describe the rheology. We can apply this frictional description of the rheology to pressure-driven channel flow in a similar way as we did for the relative viscosity, by looking at the local values. The viscous number is defined as the local viscous shear stress over the local wall-normal particle stress according to:

$$I_v = \frac{\frac{1}{\mathrm{Re}_b (d/2H)}\left|\frac{\partial \overline{\langle v_m \rangle}}{\partial z}\right|}{-\overline{\langle \sigma_{p,22} \rangle}}. \tag{31}$$

In this approach, a macroscopic friction coefficient μ is used instead of the shear viscosity of the suspensions. This friction coefficient is defined as the local total shear stress over the local wall-normal particle stress according to:

$$\mu = \frac{\frac{1}{\mathrm{Re}_b (d/2H)} |\frac{\partial \overline{\langle v_m \rangle}}{\partial z}| + |\overline{\langle \sigma_{p,12} \rangle}|}{-\overline{\langle \sigma_{p,22} \rangle}}. \tag{32}$$

For the evaluation of the $\mu(I_v)$ rheology, a region near the walls of 2 particle diameters wide is excluded to eliminate wall effects, as we also did before for the evaluation of the relative suspension viscosity. Contrary to the calculation of the relative viscosity, the core of the channel is included for the frictional rheology description because the normal particle stress remains finite (nonzero) throughout the domain.

The macroscopic friction coefficient as a function of the viscous number is shown in Fig. 19a. This shows that each case describes a viscous number range that shifts toward lower I_v with increasing volume fraction. With this shifting range, the data of the different simulation cases collectively describe a curve similar to the models proposed in literature [5,18,38], shown by the black lines. However, there is a deviation from the models at low viscous number for all the cases, corresponding to the core region. For small I_v, $\mu < \mu_1 \approx 0.3$ and the macroscopic friction coefficient is thus lower than the minimum value found for simple shear flows, which is referred to as "subyielding" by Gillissen and Ness [26]. Subyielding starts at lower I_v for higher ϕ_b and higher μ_c, related to a stronger wall-normal particle stress and hence lower I_v at the edges of the core region where the homogeneous shear flow rheology based on the mean shear rate breaks down. The model fitted in our previous work to DNS data for simple shear flow [11], shown by the colored dashed lines, shows a better agreement for high viscous numbers, but follows the same trend as the other models from literature. The colored solid lines show the result from a modified model, which will be discussed later.

Figure 19b depicts the normalized local volume fraction as a function of the viscous number. Over the entire range of viscous numbers, the data show a behavior similar to the models in literature [5,18,38], with a collapse of the data for high viscous numbers. However, the deviation of our data from the model predictions is also evident here for low viscous number. For the case with $\phi_b = 0.5$ and $\mu_c = 0.5$, $\bar{\phi}/\phi_m = 1.027 > 1$ for small I_v, thus indicating the presence of "overcompaction" [26] in the core. For the other cases shown in Fig. 19b, the maximum concentration is lower than ϕ_m. This indicates that for lower ϕ_b and/or lower μ_c, shear migration is not strong enough to cause jamming of the suspension flow in the core, contrary to the jamming prediction of the suspension balance model as discussed in the introduction. The modified frictional rheology model of Lecampion and Garagash [25], given by Eqs. (9a) and (9b), allows for subyielding and overcompaction, but suffers from the problem that it *always* results in overcompaction in the core region, irrespective of the values for the bulk volume fraction and Coulomb friction coefficient (see, e.g., Fig. 6b in their manuscript).

The scatter at low viscous number in Fig. 19a, b, is caused by the dense particle plug in the center of the channel that has developed due to shear-induced particle migration, with a maximum local volume fraction that does not scale with the maximum flowable packing fraction. Inside this plug, the mean shear rate approaches zero at the centerline, decoupling the behavior in the plug from the maximum *flowable* packing fraction ϕ_m that is used to scale the rheology in the model of Boyer et al. [18]. To possibly improve the extension of the homogeneous frictional rheology model to pressure-driven channel flow with heterogeneous shear, we first need to know the cause of the deviation of our data from existing homogeneous shear rheology models. Therefore, similar to the decomposition of the relative shear viscosity shown in Fig. 15, we decomposed the macroscopic friction coefficient into the hydrodynamic part, μ^h, and the contact part, μ^c, which are shown in Fig. 19c, d, respectively. The hydrodynamic contribution shows a very good collapse of the data down to low viscous numbers, where there is a larger spread on the data, but no clear consistent deviation from the existing models; the presence of two different branches in our data points for small I_v is related to a small asymmetry and slight lack of statistical convergence of the flow in the core region. It appears that our data for the hydrodynamic part can be well described by the model of Gallier et al. [5] given by Eq. (8). The value of ϕ_m used in this model, is based on the Maron–Pierce fit to the relative shear viscosity shown in Fig. 14b. The fits to the model of Gallier et al. [5] are shown in Fig. 19c by the dashed and solid black lines (without markers) for $\mu_c = 0$ and $\mu_c = 0.5$, respectively, and show a good description of the data. The model coefficients are shown in Table 5.

Looking at the contact contribution in Fig. 19d, it immediately becomes clear that the deviation from the homogeneous shear rheology at low I_v is caused by a strong decrease in μ^c. Where the contact contribution in simple (homogeneous) shear flow reaches a constant plateau value at low viscous number, which is described

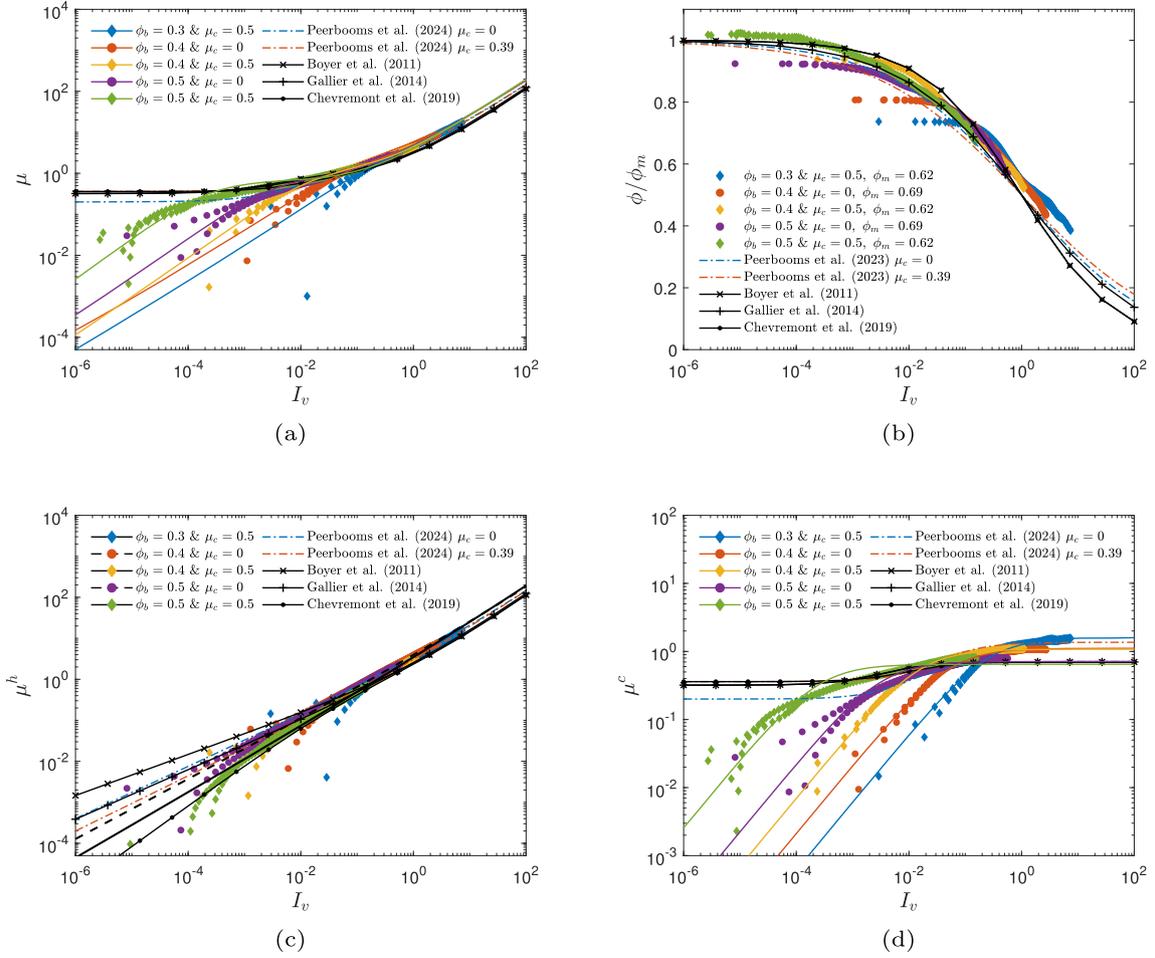**Fig. 19** Local frictional rheology as a function of the viscous number I_v. **a** Macroscopic friction coefficient μ. **b** Normalized solid volume fraction $\bar{\phi}/\phi_m$. **c** Hydrodynamic contribution to the macroscopic friction coefficient, μ^h, and **d** contact contribution to the macroscopic friction coefficient, μ^c. Lines show model descriptions as specified in the legends of the figures

in existing models by means of a normalized yield stress μ_1, this plateau is not visible in our data. The easiest modification we can make, is to eliminate the lower plateau from the homogeneous shear rheology model of Boyer et al. [18] leading to:

$$\mu^c = \frac{\mu_2^p}{1 + I_0^p/I_v},\tag{33}$$

where the superscript p denotes pressure-driven flow. Fitting this equation to the different simulation cases gives a reasonable description of the data that accounts for the decrease at low I_v and is shown by the colored solid lines in Fig. 19d. Equation (33) captures the behavior of μ well for low I_v and reasonably well for the intermediate I_v range where the transition occurs toward subyielding. The values of the model coefficients, μ_2^p and I_0^p, are given in Table 5. Together with the model of Gallier et al. [5] for the hydrodynamic part, our modified model for the contact contribution is able to describe the macroscopic friction coefficient as a function of the viscous number across the entire channel, as shown by the colored solid lines in Fig. 19a, including subyielding in the core region:

$$\mu = \frac{\mu_2^p}{1 + I_0^p/I_v} + I_v + [\eta]\phi_m I_v^{1-n}.\tag{34}$$

Table 5 Fitting coefficients for the frictional rheology model for pressure-driven channel flow compared to the coefficients for simple shear flow from previous work [11] and literature [5,18,38]

	$\mu_c = 0$		$\mu_c = 0.5$			Peerbooms et al. [11]			Boyer et al. [18]	Gallier et al. [5]	Chèvremont et al. [38]
						$\mu_c = 0$	$\mu_c = 0.2$	$\mu_c = 0.39$			
ϕ_b	0.4	0.5	0.3	0.4	0.5						
ϕ_m	0.69		0.625			0.72	0.69	0.67	0.585	0.64	$f(\mu_c)$
n	0.272		0.209			0.366	0.342	0.331	0.5	0.4	0.5
$[\eta]$	4.27		3.91			3.53	3.27	3.07	2.5	2.4	2.5
μ_1	0	0	0	0	0	0.2	0.3	0.36	0.32	0.32	0.36
μ_2	1.112	0.711	1.598	1.078	0.648	0.71	0.88	1.04	0.7	0.7	0.7
I_0	0.0526	0.0032	0.262	0.0154	2.5e-4	0.0194	0.0368	0.0584	0.005	0.005	0.0133

Our model predicts that subyielding sets in below a critical viscous number given by:

$$I_v^{sub} \approx \frac{I_0^p}{(\mu_2^p/\mu_1^h - 1)}, \tag{35}$$

where μ_1^h denotes the limiting value of μ for small I_v in the case of homogeneous shear flow and where we assumed that the hydrodynamic contribution is negligible for small I_v. Furthermore, for $I_v/I_0^p \ll 1$, subyielding is characterized by an approximately linear relationship for the macroscopic friction coefficient given by:

$$\mu \approx \frac{\mu_2^p}{I_0^p} I_v. \tag{36}$$

The fitting parameters I_0^p and μ_2^p vary with the bulk solid volume fraction and the solid friction coefficient. Figure 20a shows that I_0^p can be described by an exponential decay as a function of ϕ_b/ϕ_m with a collapse of all cases:

$$I_0^p = ae^{-b(\phi_b/\phi_m)}, \tag{37}$$

with $a = 4.62 \cdot 10^3$ and $b = 20.1$ coefficients obtained from a least-squares fit to the data. Figure 20b shows that μ_2^p decreases linearly with the bulk solid volume fraction:

$$\mu_2^p = a\phi_b + b, \tag{38}$$

with $a = -4.53$ and $b = 2.93$ coefficients obtained from a least-squares fit to the data. Interestingly, we can also describe the centerline value of the solid volume fraction by a linear relation with the bulk solid volume fraction, as shown in Fig. 20c. A least-squares fit to the data yields:

$$\phi_p = a\phi_b + b, \tag{39}$$

where a = 0.87 and b = 0.21 coefficients obtained from a least-squares fit to the data. Instead of using the bulk volume fraction, we can therefore use Eq. (39) to express I_0^p as a function of ϕ_p/ϕ_m and ϕ_m and μ_2^p as a function of ϕ_p.

To complete the description of the frictional rheology for pressure-driven channel flow, a relation between the volume fraction and the viscous number is needed. The existing models from literature based on Eq. (6), with ϕ_m obtained from fitting the Maron–Pierce correlation to the relative shear viscosity data, do not satisfy our data due to the deviation at low I_v, as is clear from Fig. 19b. Inside the central plug region the local volume fraction is independent of I_v and given by Eq. (39), while outside the central plug region the model of Boyer et al. [18] for homogeneous shear flow, Eq. (6), provides a good description of the data. Because the transition to the plateau value is smooth and occurs at different I_v and $\bar{\phi}$ for each simulated case, it is not straightforward to accurately define the edge of the plug from Fig. 19b. Instead, we turn to the suspension behavior itself to define this transition.

Inside the central plug region, the mean shear rate goes to zero when approaching the centerline, while shear stress fluctuations remain present. This motivates to introduce an 'rms shear' viscous number, Θ_v, based on the rms of the fluctuating viscous shear stress with the rms shear rate estimated from the ratio of the square root
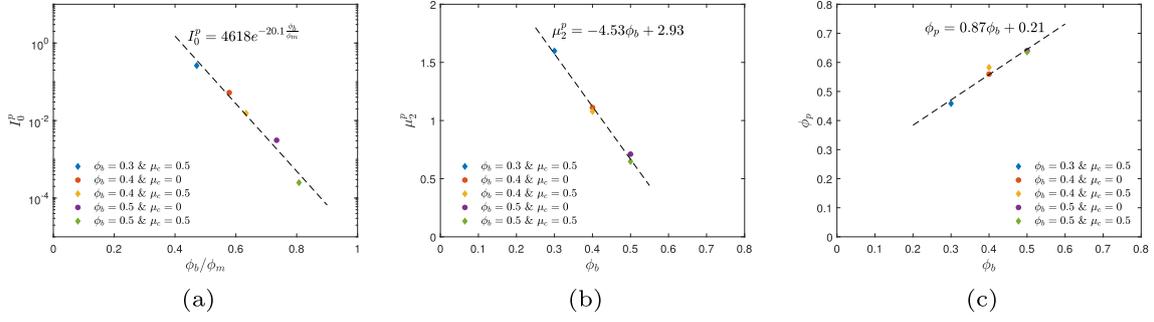
Fig. 20 Scaling of the fitting parameters, **a** I_0^P and **b** μ_2^p for the modified frictional rheology model and **c** the peak solid volume fraction in the core, ϕ_p

of the so-called granular temperature, $\sqrt{T_g}$, and the particle diameter, d; this proxy is similar to the 'granular fluidity parameter' in the study by Zhang and Kamrin [48]. In non-dimensional form, Θ_v is given by:

$$\Theta_v = \frac{\sqrt{T_g}/(\mathrm{Re}_b(d/2H))}{-\overline{\langle\sigma_{p,22}\rangle}}, \tag{40a}$$

where it is noted that $\sqrt{T_g}$ is normalized with v_b and $\sigma_{p,22}$ is normalized with $\rho_f v_b^2$. The granular temperature is a measure for the kinetic energy per unit mass of the fluctuating particle motions and defined as:

$$T_g = 0.5(u_{p,\mathrm{rms}}^2 + v_{p,\mathrm{rms}}^2 + w_{p,\mathrm{rms}}^2), \tag{40b}$$

where $u_{p,\mathrm{rms}}^2 = \overline{\langle(u_p - \overline{\langle u_p\rangle^p})^2\rangle^p}$ is the variance of the particle velocity in the x direction, and $v_{p,\mathrm{rms}}^2$ and $w_{p,\mathrm{rms}}^2$ are the variances in, respectively, the y and the z direction and defined in a similar way. In Fig. 21a, the 'rms shear' viscous number (Θ_v) is plotted as a function of the 'mean shear' viscous number (I_v). For sufficiently high I_v, Θ_v increases nearly linearly with I_v, related to stronger particle velocity fluctuations for higher mean shear rate, and is independent of the Coulomb friction coefficient. For small I_v, corresponding to the central core region, Θ_v is constant in I_v, with the constant being smaller for higher ϕ_b and higher μ_c. The plateau value is plotted in Fig. 21b and appears to decay exponentially as a function of ϕ_b/ϕ_m. Based on Fig. 20a, b, we model Θ_v according to:

$$\Theta_v = \begin{cases} 0.30(I_v^*)^{0.85} & \text{for} \quad I_v \leq I_v^* \\ 0.30(I_v)^{0.85} & \text{for} \quad I_v \geq I_v^* \end{cases}, \tag{41a}$$

where I_v^* is the value of I_v at which Θ_v undergoes a transition from a constant value to a power-law function in I_v. I_v^* is given by:

$$I_v^* = 480.6\, e^{-13.4\frac{\phi_b}{\phi_m}}. \tag{41b}$$

Interestingly, I_0^p in the frictional rheology model appears closely related to I_v^* according to:

$$I_0^p = 0.44(I_v^*)^{1.5}. \tag{42}$$

Figure 22a confirms this correlation, except for the case with $\phi_b = 0.5$ and $\mu_c = 0.5$, which clearly deviates from the trend. In Fig. 22b, I_v^* and I_v^{sub} from Eq. (35) are depicted as a function of ϕ_b/ϕ_m. Both I_v^* and I_v^{sub} show the same decaying trend for increasing bulk concentration. I_v^* is roughly a factor 15 larger than I_v^{sub} for $\phi_b = 0.2 - 0.4$, while at $\phi_b = 0.5$ and $\mu_c = 0.5$ they collapse. It is not clear what causes the deviation for the case with $\phi_b = 0.5$ and $\mu_c = 0.5$ in Fig. 22a, b, but it might be related to the overcompaction that is observed only for this particular case.

In Fig. 23, the normalized local mean volume fraction, $\bar{\phi}/\phi_m$, is plotted as a function of Θ_v. Outside the central core region, the data collapse onto a single curve, as expected since both $\bar{\phi}/\phi_m$ and Θ_v scale with I_v here. However, in the central core region, corresponding to the low I_v range in each dataset, the data do clearly not collapse.
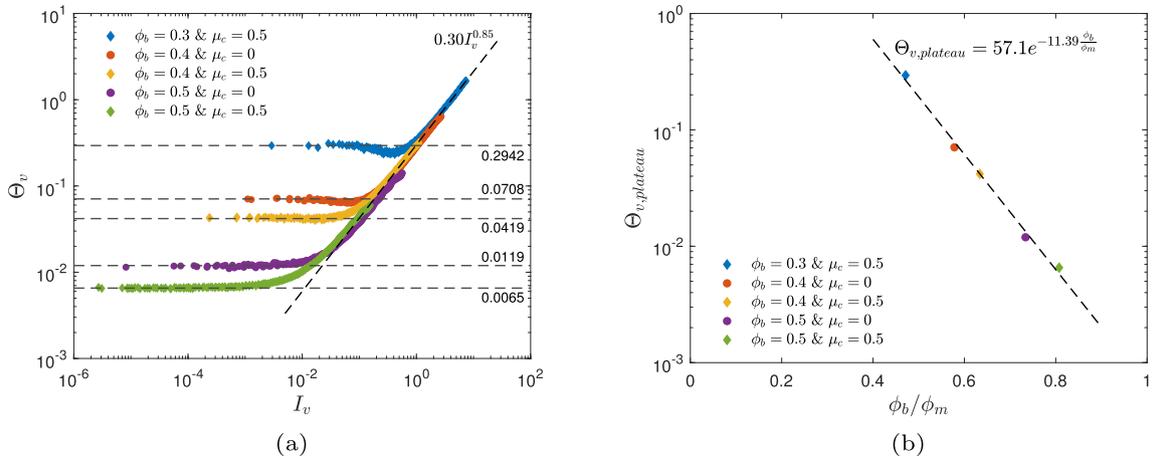
Fig. 21 **a** Rms shear viscous number, Θ_v, as a function of the mean shear viscous number, I_v, and **b** $\Theta_{v,plateau}$ as a function of ϕ_b/ϕ_m
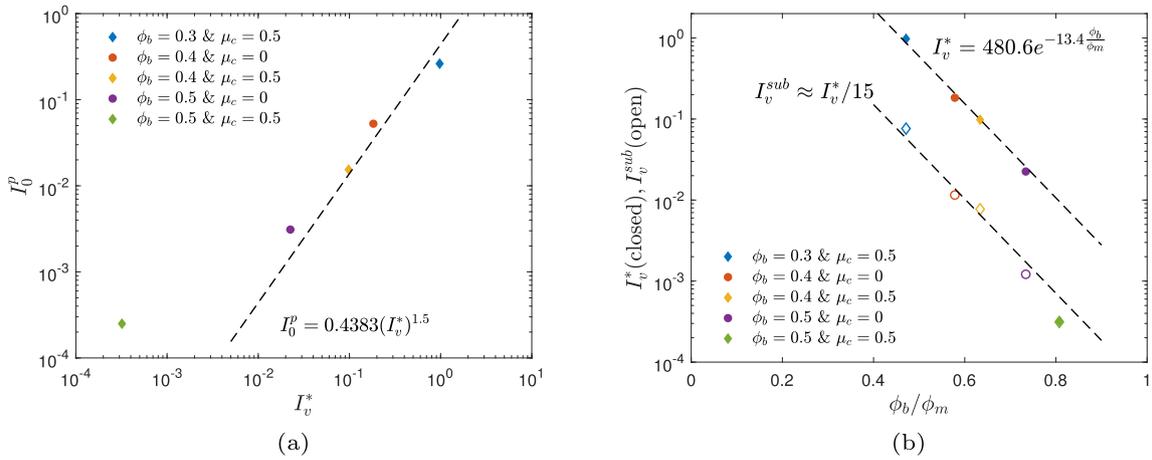

Fig. 22 **a** I_0^p as a function of I_v^* and **b** I_v^* and I_v^{sub} as a function of ϕ_b/ϕ_m. Note that I_v^* and I_v^{sub} coincide for the case with $\phi_b = 0.5$ and $\mu_c = 0.5$
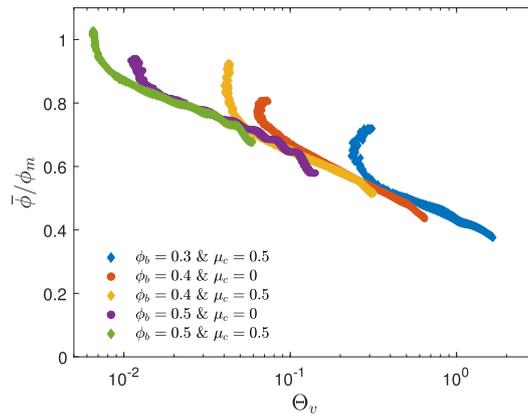

Fig. 23 Local mean volume fraction normalized with the maximum flowable packing fraction, $\bar{\phi}/\phi_m$, as a function of the 'rms shear' viscous number, Θ_v
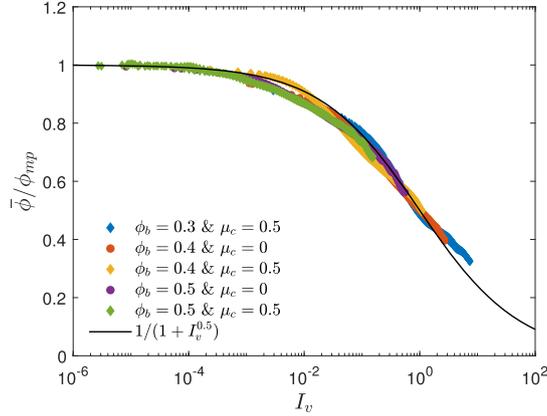
Fig. 24 Local mean volume fraction normalized with the modified maximum flowable packing fraction, $\bar{\phi}/\phi_{mp}$, as a function of the 'mean shear' viscous number, I_v

Interestingly, we found that the data for the local mean volume fraction can be collapsed by introducing a *modified* maximum flowable packing fraction given by:

$$\phi_{mp} = \phi_p \left(1 - \left(\frac{\Theta_v}{I_v}\right)^q\right) + \phi_m \left(\frac{\Theta_v}{I_v}\right)^q, \tag{43}$$

where Θ_v/I_v is a proxy for the ratio of the rms to the mean shear rate and where q is an adjustable parameter. In Fig. 24, $\bar{\phi}/\phi_{mp}$ is plotted as a function I_v for $q = -0.3$. We find that this value for q yields the best collapse of the data onto a single curve given by Eq. (6) with ϕ_m replaced by ϕ_{mp}:

$$\bar{\phi} = \frac{\phi_{mp}}{1 + I_v^{0.5}}. \tag{44}$$

Based on the parameterization of Θ_v as a function of I_v, Eq. (43) for ϕ_{mp} can be rewritten according to:

$$\phi_{mp} = \begin{cases} \phi_p - 1.44(\phi_p - \phi_m)(I_v^*)^{0.045}\left(\frac{I_v}{I_v^*}\right)^{0.3} & \text{for } \frac{I_v}{I_v^*} \leq 1 \\ \phi_m + (\phi_p - \phi_m)\left[1 - 1.44 I_v^{0.045}\right] & \text{for } \frac{I_v}{I_v^*} \geq 1 \end{cases}. \tag{45}$$

In the limit of $I_v/I_v^* \to 0$, $\phi_{mp} \to \phi_p$. For $I_v/I_v^* \geq 1$ and $I_v = 1$, $\phi_{mp} \approx \phi_m$ when $\phi_b \approx 0.55$ for $\mu_c = 0$ and when $\phi_b \approx 0.48$ for $\mu_c = 0.5$. It thus appears that $I_v = I_v^*$ marks the transition between the central core region with low mean shear and possible overcompaction (such as for the case with $\phi_b = 0.5$ and $\mu_c = 0.5$), and the 'flowable' region in which the rheology is similar to the rheology for homogeneous shear flows.

4 Conclusions

We have presented results from particle-resolved DNS of dense frictionless and frictional suspensions of non-colloidal, monodisperse and neutrally buoyant spheres in viscous pressure-driven channel flow. The channel height was equal to 20 particle diameters. The bulk solid volume fraction was varied in the range of $\phi_b = 0.2 - 0.6$ and two different Coulomb friction coefficients were considered, $\mu_c = 0$ and 0.5. In our study, we focused on the influence of ϕ_b and μ_c on the flow development and on heterogeneous shear effects on the steady-state rheology. Our main findings are summarized below.

Starting from an initially homogeneous particle distribution and the pure fluid flow velocity profile, the particle phase showed shear-induced migration toward the core till equilibrium was reached with a concentration peak at the channel centerline and a blunted mean velocity profile. From the concentration profile, the flow development time, t_{dev}, was determined by introducing an evolution parameter and fitting an exponentially decaying function in time to the data in a similar manner as in Hampton et al. [28]. The development time scales with $H^3/(v_b(d/2)^2)$ and decays exponentially with increasing bulk concentration normalized with a friction-dependent reference concentration, ϕ_b/Φ_R, where $\Phi_R \approx 0.165$ for $\mu_c = 0$ and $\Phi_R \approx 0.127$ for

$\mu_c = 0.5$. The reference concentration is interpreted as the bulk concentration beyond which particle contacts are responsible for a rapid increase in the wall-normal particle stress with increasing ϕ_b, resulting in faster shear-induced migration.

At statistically steady state, three distinct regions can be distinguished in the flow: a wall-affected region with a thickness of $2 - 3$ particle diameters and characterized by pronounced particle layering induced by the wall flatness, a dense plug (low-shear) flow region in the core, and an intermediate shear region in which the mean velocity and concentration are gradually increasing from the wall toward the core region. For the highest investigated bulk concentration ($\phi_b = 0.6$), wall-induced layering extended throughout the entire domain, and hence these cases were ignored in the analysis of the suspension rheology. Furthermore, for the lowest investigated bulk concentrations ($\phi_b = 0.2$ & $\phi_b = 0.3$ with $\mu_c = 0$), the flow development time was too long and the simulations had to be stopped before statistical equilibrium was reached. Hence, the steady-state rheology analysis was based only on bulk concentrations in the range of $\phi_b = 0.3 - 0.5$.

Based on the particle pair distribution function (PPDF), the suspension microstructure in the intermediate region was found to be similar to the PPDFs found for simple (homogeneous) shear flows and characterized by clear depletion zones along the extensional axis of the flow around the particles. These depletion zones are absent in the microstructure in the core region, related to the nearly uniform (low-shear) plug flow here. Furthermore, in the core, the particles preferentially align themselves in the streamwise direction for $\phi \geq 0.4$ without a discernable effect of particle friction, likely related to the collective motion of the particles.

We have analyzed the 'viscous' rheology for the intermediate region. In this flow region, the local relative shear viscosity, η/η_0, scales well with the local concentration normalized with the maximum flowable packing fraction, $\bar{\phi}/\phi_m$, similar to the scaling observed for simple shear flow. Based on fitting the Maron–Pierce correlation to the DNS data, we obtained $\phi_m \approx 0.69$ for $\mu_c = 0$ and $\phi_m \approx 0.62$ for $\mu_c = 0.5$, consistent with the values we previously found for plane Couette flow [11]. The contribution from particle contacts to the relative shear viscosity is dominant beyond $\bar{\phi}/\phi_m \approx 0.7$. The hydrodynamic contribution dominates for smaller volume fractions. This contribution actually scales better with $\bar{\phi}$ rather than $\bar{\phi}/\phi_m$ over the entire range of volume fractions, and is independent of μ_c.

In the intermediate region, the normalized normal stress differences, N_1 and N_2 divided by the local total shear stress, appear to scale fairly well with $\bar{\phi}/\phi_m$, but remain explicitly dependent on μ_c. The results are generally in good agreement with previous results obtained for plane Couette flow [11], though a stronger decrease toward more negative values is observed for high volume fractions in the N_2 data. We also fitted empirical correlations proposed by Badia et al. [45] to the normal stresses, from which the normal stress differences can be fairly well estimated, in particular N_2. The normal stress anisotropy coefficients, λ_2 and λ_3, both scale fairly well with $\bar{\phi}/\phi_m$ and show little dependence on μ_c.

We have analyzed the 'frictional' rheology for the combination of the intermediate region and the core region. For the higher viscous number (I_v) range, the macroscopic friction coefficient (μ) exhibits similar behavior as in simple shear flow. However, for low I_v, 'subyielding' is present with μ decreasing approximately linearly with decreasing I_v at fixed ϕ_b and μ_c. Similarly, for the higher I_v range, $\bar{\phi}/\phi_m$ scales with I_v as in simple shear flow, while for $I_v \to 0$ the behavior of $\bar{\phi}/\phi_m$ is different from simple shear flow. In the core region, we observed 'overcompaction' beyond ϕ_m for the case with $\phi_b = 0.5$ and $\mu_c = 0.5$, while for the other cases at lower ϕ_b and/or $\mu_c = 0$ the maximum core concentration is lower than ϕ_m.

From the decomposition of μ into a hydrodynamic and a contact contribution, we found that subyielding at low I_v originates from a change in the contact contribution with respect to simple shear flow. We presented a modified frictional rheology model that accounts for subyielding in the core region. The macroscopic friction coefficient μ is given by Eq. (34). Correlations for the model coefficients, I_0^p and μ_2^p, are given by Eqs. (37) and (38), respectively. The relation between the local solid volume fraction and the viscous number I_v is described well by Eq. (44), where ϕ_{mp} is the modified maximum flowable packing fraction defined by Eq. (43). Based on our results, ϕ_{mp} can be modeled according to Eq. (45), combined with Eq. (39) for the maximum core packing fraction, ϕ_p, and Eq. (41b) for I_v^*. This closes our frictional rheology model for pressure-driven channel flow. This model is able to capture both possible overcompaction in the core region as well as maximum core concentrations below the jamming limit for lower bulk volume fractions.

Compared to frictional rheology models for simple shear flows, key features of the present model for pressure-driven channel flow are: (1) the absence of a yield stress for $I_v \to 0$, (2) the inclusion of the mean-to-rms shear-rate ratio, I_v/Θ_v, into the model to distinguish between the low-shear plug flow in the core region and the sheared suspension flow in the intermediate region. The transition between the two regions is effectively controlled by the I_v^* parameter, which represents the value of I_v below which shear-stress fluctuations become decoupled from the local mean shear rate.

In order to validate our proposed frictional rheology model further, a larger range of the Coulomb friction coefficient may be investigated. This would improve the accuracy of the parameterization of the model coefficients. Also, the effects of polydispersity in particle size and shape would be interesting to examine, to be able to model more realistic suspensions in the future. Furthermore, the influence of the particle-to-channel size ratio should be explored further. For the steady-state rheology, we do not expect a strong effect of particle size on the suspension rheology in the intermediate channel region, where the suspension behavior is similar as in homogeneous shear flows. Particle size is expected to have an influence though on wall layering and the central core region as well as on the granular temperature [20].

Finally, it would be interesting to use the modified frictional rheology description to improve the suspension balance model (SBM) discussed in the introduction. To compare SBM predictions with the DNS results, still a carefully validated constitutive model for the normal particle stress is required. Our DNS results indicate non-local suspension behavior in the channel core, where the wall-normal particle stress remains nonzero while the 'mean shear' viscous number (I_v) approaches zero at the centerline as dictated by statistical flow symmetry. It is precisely for this reason that the classical SBM formulation predicts a peak volume fraction at the channel centerline equal to the maximum flowable packing fraction. Interestingly, our results show that the 'rms shear' viscous number (Θ_v) based on the square root of the granular temperature, does remain nonzero, and we proposed a correlation for the plateau value reached in the central core region, see (41a). Furthermore, outside the central core region, the rms shear viscous number appears fully correlated with the mean shear viscous number through a power-law relation. These findings support the suggestion of Nott and Brady [20] to base the constitutive relation for the wall-normal particle stress on the fluctuating shear rate, $\sqrt{T_g}/d$, instead of the mean shear rate, $|\partial \overline{v}_m / \partial z|$, or, alternatively, as a function of both. This requires the extension of the SBM with an additional energy equation for the granular temperature. This approach has been shown already to overcome the problem of the classical SBM with the packing fraction at the channel centerline [20]. It is left for future study to explore such constitutive modeling and validation of the SBM in more detail.

Data availability The data that support the findings of this study are openly available in 4TU.ResearchData repository at https://doi.org/10.4121/e7c86771-72bb-48da-b9f9-6c0857655404 [49].

Declarations

Conflict of interest The authors declare that they have no conflict of interest.

Appendix A Example of determination of different flow regions for calculation of the PPDFs

Figure 25 shows the determination of the different flow regions in the domain for the calculation of the PPDF for the case with $\phi_b = 0.4$ and $\mu_c = 0$. Figure 25a shows the mean intrinsic fluid velocity and its wall-normal derivative. The edge of the core region is defined as the location where $|\partial(\overline{\langle v_f \rangle^f}/v_b)/\partial(z/d)|$ drops below 0.04. In Fig. 25b, this region is displayed on the concentration profile, together with the edge of the wall region at three particle diameters from the wall. The intermediate region is defined by $3 \leq z/d \leq z_{\text{core}}/d$.

Appendix B Example of local relative viscosity calculation

For the case with $\phi_b = 0.4$ and $\mu_c = 0$, Fig. 26 shows the relative shear viscosity as a function of the wall-normal coordinate for the region considered for the calculation (a) and the corresponding concentration profile
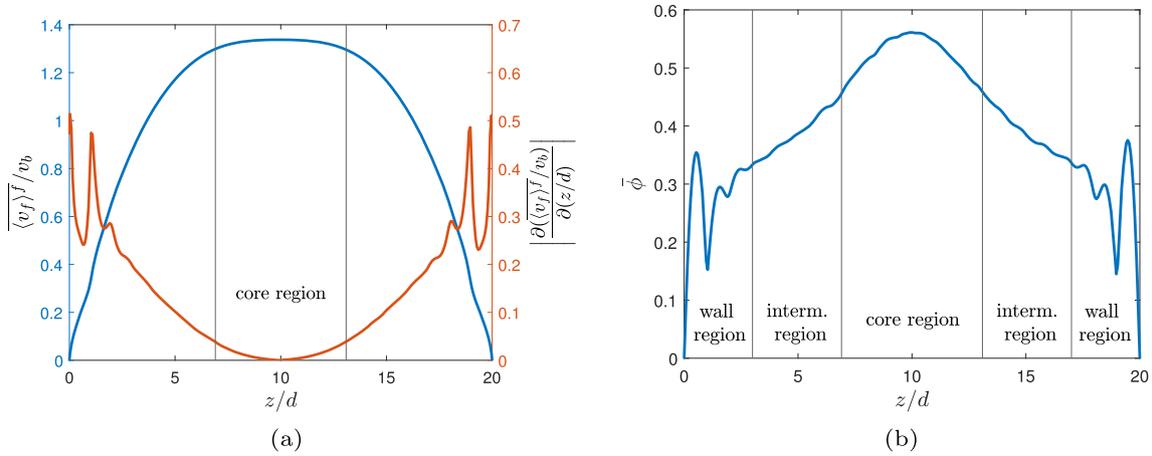
Fig. 25 Determination of the different flow regions in the domain for calculation of PPDFs for the case with $\phi_b = 0.4$ and $\mu_c = 0$. **a** The mean intrinsic fluid velocity and its wall-normal derivative used to determine the extent of the core region. **b** The mean solid volume concentration as a function of the wall-normal coordinate with the vertical lines delineating the boundaries of the different flow regions
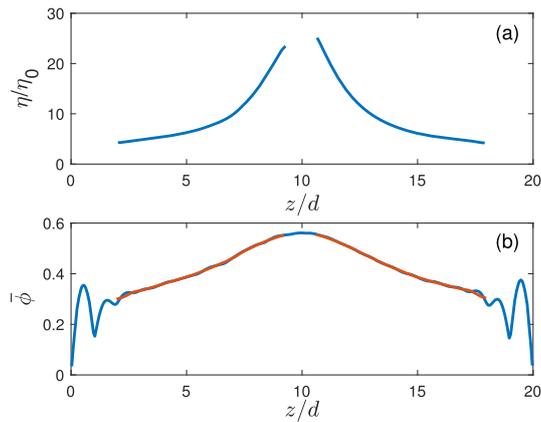

Fig. 26 Relative shear viscosity as a function of the wall-normal coordinate for the case with $\phi_b = 0.4$ and $\mu_c = 0$, shown for the regions that are included in the calculation (**a**), and the corresponding concentration profile in blue with a smoothed profile in red for the included regions (**b**). Smoothing of the concentration profile is done using a moving average with a width of one particle diameter

in blue with a smoothed profile shown in red (b). The smoothing of the concentration profile is done using a moving average with a width of one particle diameter. This smoothing is also used for the stress profiles in the analysis of the frictional rheology. The region that is excluded near the wall, is 2 particle diameters wide to avoid contamination of the results by wall layering effects. The width of the excluded region in the center of the channel is determined by the local value of the viscous shear stress. The viscous shear stress goes through zero in the center of the channel, causing a singularity in the relative viscosity as can be seen from Eq. (27). To avoid this we have chosen to exclude the region where the viscous shear stress drops below a value of $|\langle\sigma_{visc,12}\rangle|/\eta_0\dot{\gamma}_w < 9e^{-3}$.

References

1. Stickel, J.J., Powell, R.L.: Fluid mechanics and rheology of dense suspensions. Annu. Rev. Fluid Mech. **37**, 129–149 (2005)
2. Pednekar, S., Chun, J., Morris, J.F.: Bidisperse and polydisperse suspension rheology at large solid fraction. J. Rheol. **62**(2), 513–526 (2018)
3. Sierou, A., Brady, J.F.: Rheology and microstructure in concentrated noncolloidal suspensions. J. Rheol. **46**(5), 1031–1056 (2002)
4. Seto, R., Mari, R., Morris, J.F., Denn, M.M.: Discontinuous shear thickening of frictional hard-sphere suspensions. Phys. Rev. Lett. **111**(21), 218301 (2013)

5. Gallier, S., Lemaire, E., Peters, F., Lobry, L.: Rheology of sheared suspensions of rough frictional particles. J. Fluid Mech. **757**, 514–549 (2014)
6. Mari, R., Seto, R., Morris, J.F., Denn, M.M.: Shear thickening, frictionless and frictional rheologies in non-Brownian suspensions. J. Rheol. **58**(6), 1693–1724 (2014)
7. Singh, A., Mari, R., Denn, M.M., Morris, J.F.: A constitutive model for simple shear of dense frictional suspensions. J. Rheol. **62**(2), 457–468 (2018)
8. Guazzelli, É., Pouliquen, O.: Rheology of dense granular suspensions. J. Fluid Mech. **852**, P1 (2018)
9. Silbert, L.E., Ertaş, D., Grest, G.S., Halsey, T.C., Levine, D.: Geometry of frictionless and frictional sphere packings. Phys. Rev. E **65**(3), 031304 (2002)
10. Fernengel, J., Hinrichsen, O.: Influence of material properties on voidage of numerically generated random packed beds. Chem. Eng. Sci. **233**, 116406 (2021)
11. Peerbooms, W., Nadorp, T., Heijden, A., Breugem, W.-P.: Interparticle friction in sheared dense suspensions: comparison of the viscous and frictional rheology descriptions. J. Rheol. **68**(2), 263–283 (2024)
12. Einstein, A.: Eine neue Bestimmung der Moleküldimensionen. PhD thesis, ETH Zurich (1905)
13. Einstein, A.: Berichtigung zu meiner Arbeit: Eine neue Bestimmung der Moleküldimensionen. Ann. Phys. **339**(3), 591–592 (1911)
14. Batchelor, G., Green, J.: The determination of the bulk stress in a suspension of spherical particles to order c^2. J. Fluid Mech. **56**(3), 401–427 (1972)
15. Krieger, I.M., Dougherty, T.J.: A mechanism for non-Newtonian flow in suspensions of rigid spheres. Trans. Soc. Rheol. **3**(1), 137–152 (1959)
16. Eilers, H.: Die Viskosität von Emulsionen hochviskoser Stoffe als Funktion der Konzentration. Kolloid-Zeitschrift **97**(3), 313–321 (1941)
17. Maron, S.H., Pierce, P.E.: Application of Ree–Eyring generalized flow theory to suspensions of spherical particles. J. Colloid Sci. **11**(1), 80–95 (1956)
18. Boyer, F., Guazzelli, É., Pouliquen, O.: Unifying suspension and granular rheology. Phys. Rev. Lett. **107**(18), 188301 (2011)
19. Leighton, D., Acrivos, A.: The shear-induced migration of particles in concentrated suspensions. J. Fluid Mech. **181**, 415–439 (1987)
20. Nott, P.R., Brady, J.F.: Pressure-driven flow of suspensions: simulation and theory. J. Fluid Mech. **275**, 157–199 (1994)
21. Morris, J.F., Boulay, F.: Curvilinear flows of noncolloidal suspensions: the role of normal stresses. J. Rheol. **43**(5), 1213–1237 (1999)
22. Nott, P.R., Guazzelli, E., Pouliquen, O.: The suspension balance model revisited. Phys. Fluids **23**(4), 043304 (2011)
23. Jamshidi, R., Gillissen, J.J., Angeli, P., Mazzei, L.: Roles of solid effective stress and fluid-particle interaction force in modeling shear-induced particle migration in non-brownian suspensions. Phys. Rev. Fluids **6**(1), 014301 (2021)
24. Miller, R.M., Morris, J.F.: Normal stress-driven migration and axial development in pressure-driven flow of concentrated suspensions. J. Nonnewton. Fluid Mech. **135**(2–3), 149–165 (2006)
25. Lecampion, B., Garagash, D.I.: Confined flow of suspensions modelled by a frictional rheology. J. Fluid Mech. **759**, 197–235 (2014)
26. Gillissen, J.J., Ness, C.: Modeling the microstructure and stress in dense suspensions under inhomogeneous flow. Phys. Rev. Lett. **125**(18), 184503 (2020)
27. Orsi, M.: Simulation of concentrated non-brownian frictional and adhesive suspensions in linear and nonlinear flows. PhD thesis, Université Côte d'Azur (2022)
28. Hampton, R., Mammoli, A., Graham, A., Tetlow, N., Altobelli, S.: Migration of particles undergoing pressure-driven flow in a circular conduit. J. Rheol. **41**(3), 621–640 (1997)
29. Lyon, M., Leal, L.: An experimental study of the motion of concentrated suspensions in two-dimensional channel flow. Part 1. Monodisperse systems. J. Fluid Mech. **363**, 25–56 (1998)
30. Lyon, M., Leal, L.: An experimental study of the motion of concentrated suspensions in two-dimensional channel flow. Part 2. Bidisperse systems. J. Fluid Mech. **363**, 57–77 (1998)
31. Gao, C., Xu, B., Gilchrist, J.: Mixing and segregation of microspheres in microchannel flows of mono-and bidispersed suspensions. Phys. Rev. E **79**(3), 036311 (2009)
32. Gao, C., Kulkarni, S., Morris, J., Gilchrist, J.: Direct investigation of anisotropic suspension structure in pressure-driven flow. Phys. Rev. E **81**(4), 041403 (2010)
33. Oh, S., Song, Y.-Q., Garagash, D.I., Lecampion, B., Desroches, J.: Pressure-driven suspension flow near jamming. Phys. Rev. Lett. **114**(8), 088301 (2015)
34. Rashedi, A., Sarabian, M., Firouznia, M., Roberts, D., Ovarlez, G., Hormozi, S.: Shear-induced migration and axial development of particles in channel flows of non-Brownian suspensions. AIChE J. **66**(12), 17100 (2020)
35. Yeo, K., Maxey, M.R.: Numerical simulations of concentrated suspensions of monodisperse particles in a Poiseuille flow. J. Fluid Mech. **682**, 491–518 (2011)
36. Chun, B., Park, J.S., Jung, H.W., Won, Y.-Y.: Shear-induced particle migration and segregation in non-Brownian bidisperse suspensions under planar Poiseuille flow. J. Rheol. **63**(3), 437–453 (2019)
37. Di Vaira, N.J., Łaniewski-Wołłk, Ł, Johnson, R.L., Aminossadati, S.M., Leonardi, C.R.: Influence of particle polydispersity on bulk migration and size segregation in channel flows. J. Fluid Mech. **939**, A30 (2022)
38. Chèvremont, W., Chareyre, B., Bodiguel, H.: Quantitative study of the rheology of frictional suspensions: influence of friction coefficient in a large range of viscous numbers. Phys. Rev. Fluids **4**(6), 064302 (2019)
39. Richarson, J., Zaki, W.: Sedimentation and fluidisation: part 1. Trans. Inst. Chem. Eng. **31**, 35–53 (1954)
40. Breugem, W.-P.: A second-order accurate immersed boundary method for fully resolved simulations of particle-laden flows. J. Comput. Phys. **231**(13), 4469–4498 (2012)
41. Costa, P., Boersma, B.J., Westerweel, J., Breugem, W.-P.: Collision model for fully resolved simulations of flows laden with finite-size particles. Phys. Rev. E **92**(5), 053012 (2015)

42. Tschisgale, S., Kempe, T., Fröhlich, J.: A non-iterative immersed boundary method for spherical particles of arbitrary density ratio. J. Comput. Phys. **339**, 432–452 (2017)
43. Picano, F., Breugem, W.-P., Mitra, D., Brandt, L.: Shear thickening in non-Brownian suspensions: an excluded volume effect. Phys. Rev. Lett. **111**(9), 098302 (2013)
44. Blanc, F., Lemaire, E., Meunier, A., Peters, F.: Microstructure in sheared non-Brownian concentrated suspensions. J. Rheol. **57**(1), 273–292 (2013)
45. Badia, A., D'Angelo, Y., Peters, F., Lobry, L.: Frame-invariant modeling for non-Brownian suspension flows. J. Nonnewton. Fluid Mech. **309**, 104904 (2022)
46. Peters, F., Ghigliotti, G., Gallier, S., Blanc, F., Lemaire, E., Lobry, L.: Rheology of non-Brownian suspensions of rough frictional particles under shear reversal: A numerical study. J. Rheol. **60**(4), 715–732 (2016)
47. Lobry, L., Lemaire, E., Blanc, F., Gallier, S., Peters, F.: Shear thinning in non-Brownian suspensions explained by variable friction between particles. J. Fluid Mech. **860**, 682–710 (2019)
48. Zhang, Q., Kamrin, K.: Microscopic description of the granular fluidity field in nonlocal flow modeling. Phys. Rev. Lett. **118**(5), 058001 (2017)
49. Peerbooms, W., Heijden, A.E.D.M., Breugem, W.-P.: Data corresponding to the publication: "Transient behavior and steady-state rheology of dense frictional suspensions in pressure-driven channel flow". 4TU.ResearchData (2024). https://doi.org/10.4121/e7c86771-72bb-48da-b9f9-6c0857655404

Publisher's Note Springer Nature remains neutral with regard to jurisdictional claims in published maps and institutional affiliations.